The Astrophysical Journal, 939:82 (20pp), 2022 November 10 https://doi.org/10.3847/1538-4357/ac8f26

Far-ultraviolet Flares on Accreting Protostars: Weak and Classical T Tauri Stellar Pair Analysis

P. C. Hinton[1,2], Kevin France[1,2,3], Maria Gracia Batista[4], Javier Serna[5], Jesús Hernández[5], Hans Moritz Günther[6], Adam F. Kowalski[1,2,7], and P. Christian Schneider[8]

[1] Laboratory for Atmospheric and Space Physics, University of Colorado, 600 UCB, Boulder, CO 80309, USA; parker.hinton@colorado.edu
[2] Department of Astrophysical and Planetary Science, University of Colorado, 389 UCB, Boulder, CO 80309, USA
[3] Center for Astrophysics and Space Astronomy, University of Colorado, 593 UCB, Boulder, CO 80309, USA
[4] Observatorio Astronómico Nacional, Facultad de Ciencias, Universidad Nacional de Colombia, Bogotá, Colombia
[5] Universidad Nacional Autónoma de México, Instituto de Astronomía, AP 106, Ensenada 22800, BC, México
[6] MIT, Kavli Institute for Astrophysics and Space Research, 77 Massachusetts Ave., Cambridge, MA 02139, USA
[7] National Solar Observatory, University of Colorado, 3665 Discovery Drive, Boulder, CO 80303, USA
[8] Hamburg Observatory, Gojenbergsweg 112, D-21029 Hamburg, Germany

Received 2022 February 11; revised 2022 August 31; accepted 2022 September 1; published 2022 November 8

Abstract

The far-ultraviolet (FUV) emission of classical T Tauri stars (CTTSs) is known to play an important role in protoplanetary disk dispersal and giant planet formation, yet the role played by protostellar flares in these processes is largely unknown. We use nearby star-forming regions as laboratories to probe the FUV flare characteristics of CTTSs and test whether flares may be masked underneath accretion luminosity. Using AD Leo as our archetypal flare template, we pilot a novel analysis technique on three weak-lined T Tauri star (WTTS) and CTTS pairs: TWA-7/TWA Hya, RECX-1/RECX-11, and LkCa19/GM Aur. We find that flares contribute an upper limit of $0.064\% \pm 0.002\%$, $3.1\% \pm 0.1\%$, and $2.7\% \pm 0.3\%$ to the total FUV energy budgets of TW Hya, RECX-11, and GM Aur, respectively. We also present predicted CTTS flare rates, which suggest that we would expect to observe roughly one 5σ flare on each of the CTTS archival light curves. We find one 5σ flare on TW Hya with $E(1380\text{–}1745\ \text{Å}) = (6.1 \pm 0.7) \times 10^{31}$ erg, but none are found on RECX-11 or GM Aur. Longer monitoring campaigns are required to provide more concrete constraints on the FUV flare frequency of accreting protostars. Optical TESS data of the targets were also analyzed to contextualize these results. Lastly, we report the first FUV flare on a WTTS (RECX-1), which is also the most energetic FUV flare event observed with the Hubble Space Telescope to date with $E(1135\text{–}1429\ \text{Å}) = (2.1 \pm 0.1) \times 10^{32}$ erg.

Unified Astronomy Thesaurus concepts: Ultraviolet astronomy (1736); Classical T Tauri stars (252); T Tauri stars (1681); Weak-line T Tauri stars (1795); Hubble Space Telescope (761)

1. Introduction

Stars are born in gas-rich pockets of galaxies referred to as star-forming regions (SFRs; Bressert et al. 2010). As these pockets gravitationally collapse to form a star, they also typically form a circumstellar disk composed of gas and dust. The young star can accrete material from this disk, which generates a unique emission-line spectrum across the UV, optical, and infrared (Hartmann et al. 2016). Stars that exhibit this profile are referred to as classical T Tauri stars (CTTSs), named after the first star (T Tauri) on which this phenomenon was observed. Planets are formed from the circumstellar disk material, but the planets themselves are generally made from less than 1% of the initial disk mass (Wright et al. 2011). Instead, the disk is dispersed via a number of different mechanisms. Accretion onto the protostar is generally the most important driver of disk evolution (Hartmann et al. 1998), as well as magnetically launched jets and winds (Königl & Salmeron 2011). Photoevaporation is also considered to be an important disk dispersal mechanism, particularly for stars with intense X-ray (0.1–100 Å), extreme-ultraviolet (EUV, 100-900 Å), and far-ultraviolet (FUV, 900–2000 Å) radiation fields (Clarke 2011).

These high-energy radiation fields cause heating of the circumstellar disk, which results in pressure-driven photoevaporative winds that carry gaseous material out of the disk (see Gorti et al. 2016; Ercolano & Pascucci 2017, for recent reviews). Gorti & Hollenbach (2009) simulate the X-ray-, EUV-, and FUV-driven winds with radiative transfer and thermochemical models and find X-ray- and FUV-driven winds to dominate over accretion at about 100 au. They find a fiducial wind rate, driven by FUV photons emitted from the protostar, of $3 \times 10^{-8}\ M_{\odot}\ \text{yr}^{-1}$, which is one to two orders of magnitude greater than the EUV-driven winds, but comparable to that of the X-ray-driven winds. Thus, the FUV luminosity of the host star is an important component of photoevaporative winds and contributes to protoplanetary disk dispersal.

This has numerous implications for the formation of planets inside of these disks. For massive O and B stars, this FUV component dominates photoevaporative heating (Johnstone et al. 1998), quickly dispersing the disk and curtailing the time available for giant planet formation (Clarke 2011). For lower-mass stars, the photoevaporative winds can alter the chemistry of the disk available for giant planet formation. Photoevaporative heating effectively removes volatiles (H and He) from the surface of the disk, enhancing the dust-to-gas ratio at the midplane. For example, observations of enriched noble gases at Jupiter (Ar, Kr, and Xe) by the spacecraft Galileo have been explained by invoking photoevaporative winds

(Guillot & Hueso 2006; Ali-Dib 2017). This mechanism can also cause later-forming gas giant cores to be starved of material and has been invoked to explain the difference in the solar system's gas-rich giants (Jupiter and Saturn) and gas-poor giants (Neptune and Uranus) (Shu et al. 1993). Lastly, these winds may be capable of driving outward planetary migration (Rosotti et al. 2013). It is clear that FUV-driven photoevaporative winds are a critical piece of the puzzle when it comes to understanding the gas giants of our solar system and beyond.

The time-integrated FUV photon energy incident on the disk may be enhanced by protostellar flares. Stellar flares are denoted by sudden large increases in a star's brightness; our understanding of what causes them is primarily attributable to studies of the Sun. A solar flare is powered by reconnection events in the magnetic field (Parker 1963; Zhu et al. 2016), which result in a fast release of magnetic energy (Gold & Hoyle 1960) in the form of accelerated charged particles. The theoretical Neupert effect (Neupert 1968; Veronig et al. 2005) entails electron beams gyrating along magnetic field lines from the corona and depositing energy into the chromosphere, which, via nonthermal bremsstrahlung, results in hard X-ray, near-UV, and optical emission. The electron beams also cause chromospheric evaporation (Antonucci et al. 1984), which describes the transfer of material outward from the chromosphere, and in turn cause heating of the corona. The corona then thermally emits soft X-ray and EUV radiation, which occurs later temporally than the nonthermal radiation; this observed temporal relationship is the empirical Neupert effect (Hawley et al. 2003; Mitra-Kraev et al. 2005). High time resolution observations of flares on low-mass M dwarfs with the Galaxy Evolution Explorer (GALEX) find rough temporal simultaneity between the NUV and the FUV (Welsh et al. 2006). This suggests that the FUV emission in flares is also triggered in the chromosphere by nonthermal bremsstrahlung; however, this subject requires further consideration.

Results from the Measurements of the Ultraviolet Spectral Characteristics of Low-mass Exoplanetary Systems (MUSCLES; France et al. 2016; Loyd et al. 2018a) and Habitable Zones and M dwarf Activity across Time (HAZMAT; Loyd et al. 2018b) surveys find that flares on M stars (whether active, inactive, young, or old) could dominate their FUV energy budgets. If these findings hold true into the T Tauri phase of a star's life ($\leqslant$10 Myr old), then FUV flares could be an important driver of photoevaporative winds. In general, stars have higher levels of magnetic activity in their youth (e.g., Johnstone et al. 2021 and references therein), which results in increased flare frequency and intensity (Medina et al. 2020). However, comprehensive FUV flare frequency distributions (FFDs) of T Tauri stars have not been created. Over the $\sim$50 CTTSs observed with the International Ultraviolet Explorer (IUE; Johns-Krull et al. 2000) and more than 1 Ms of observation time of CTTSs in the FUV with the Hubble Space Telescope (HST), there has yet to be a definitive FUV flare detection reported in the literature. On the other hand, flares on CTTSs have been observed in the optical, as seen in this study and in the literature (Gullbring et al. 1995; Kóspál et al. 2018; Ansdell et al. 2016), and they are also found in X-ray data (Robrade & Schmitt 2006; Getman & Feigelson 2021).

Flare studies in the X-ray demonstrate that pre-main-sequence (PMS) stars show frequent flare events caused by magnetic activity. These X-ray flares are easily detectable compared to optical or FUV flares because their decay times are usually much longer (hours vs. minutes; e.g., Schmitt et al. 2019). Several studies have found that any individual PMS star may show a few flares per week (Wolk et al. 2005; Getman & Feigelson 2021) and that there is no significant evolution during the first 10 Myr, i.e., flare rates and energetics are indistinguishable between accreting and nonaccreting stars (e.g., Stelzer et al. 2007). Sometimes, however, subtle differences between accreting and nonaccreting stars are seen (Getman et al. 2008), but we note that these conclusions are usually drawn from low event numbers and that we consider X-ray flares to happen with the same frequency and energy on CTTSs and weak-lined T Tauri stars (WTTSs; Getman & Feigelson 2021).

The FUV flare characteristics of PMS stars are less well studied, and a lack of detected events may suggest the (non) existence of additional important physical mechanisms. Interestingly, when comparing the FUV light curve of a CTTS (Figure 4) to AD Leo, a young and active main-sequence M star (Figure 1), a lack of flares on the CTTS is immediately obvious. There are two hypotheses to explain the lack of observed flares: (1) accretion luminosity is masking the FUV flares, leading to a decreased observed flare frequency; or (2) CTTS physical conditions do not lend them to flaring, and thus the actual flare rate is decreased compared to their WTTS counterparts. We will refer to the first hypothesis as "accretion masking," and the second is hereto referred to as the "decreased flare frequency" hypothesis. A third hypothesis is that FUV extinction due to circumstellar gas on CTTSs leads to a decreased observed flare frequency. Stellar quiescent flux, magnetospheric flares, and the shocks that generate accretion luminosity all occur within a few stellar radii; thus, circumstellar extinction should affect them similarly (McJunkin et al. 2014). This mechanism is certainly a relevant factor for edge-on stars (Schneider et al. 2013, 2020), but it is a less likely explanation for the lack of observed flares on the more face-on CTTSs in the present study (Teague et al. 2019).

In this study, we test the accretion masking hypothesis by assuming that, with respect to FUV emission, the only difference between a CTTS and a WTTS is the accretion signal present in the CTTS spectrum (Gullbring et al. 1998). A CTTS becomes a WTTS once its protoplanetary disk is dispersed and mass accretion halts; the protostar is referred to as "weak-lined" owing to the weakened intensity of spectral accretion lines such as Hα. This process sets the lifetime of a CTTS and generally takes a few to 10 Myr (Alexander et al. 2014). The assumption that a CTTS can be regarded as a WTTS underneath an accretion disk reflects the conclusions of Ingleby et al. (2011) when comparing chromospheric emission of RECX-1 and RECX-11 and the findings of Getman & Feigelson (2021) in the X-ray for disk-bearing stars and diskless stars.

Under this paradigm, we identify WTTS/CTTS pairs from nearby SFRs and test whether the underlying WTTS flare signals would be detectable above the FUV accretion flux of the associated CTTSs. In order to make this comparison, given the lack of a comprehensive set of FUV observations of WTTSs, we additionally assume that WTTSs have FFDs similar to the relatively young (25–300 Myr) mid-type M star AD Leo (Hawley et al. 2003; Shkolnik et al. 2009; Loyd & France 2014). This enables us to predict the number of statistically significant FUV flares that should be observed as a function of time on each of the three pilot CTTS targets (TW

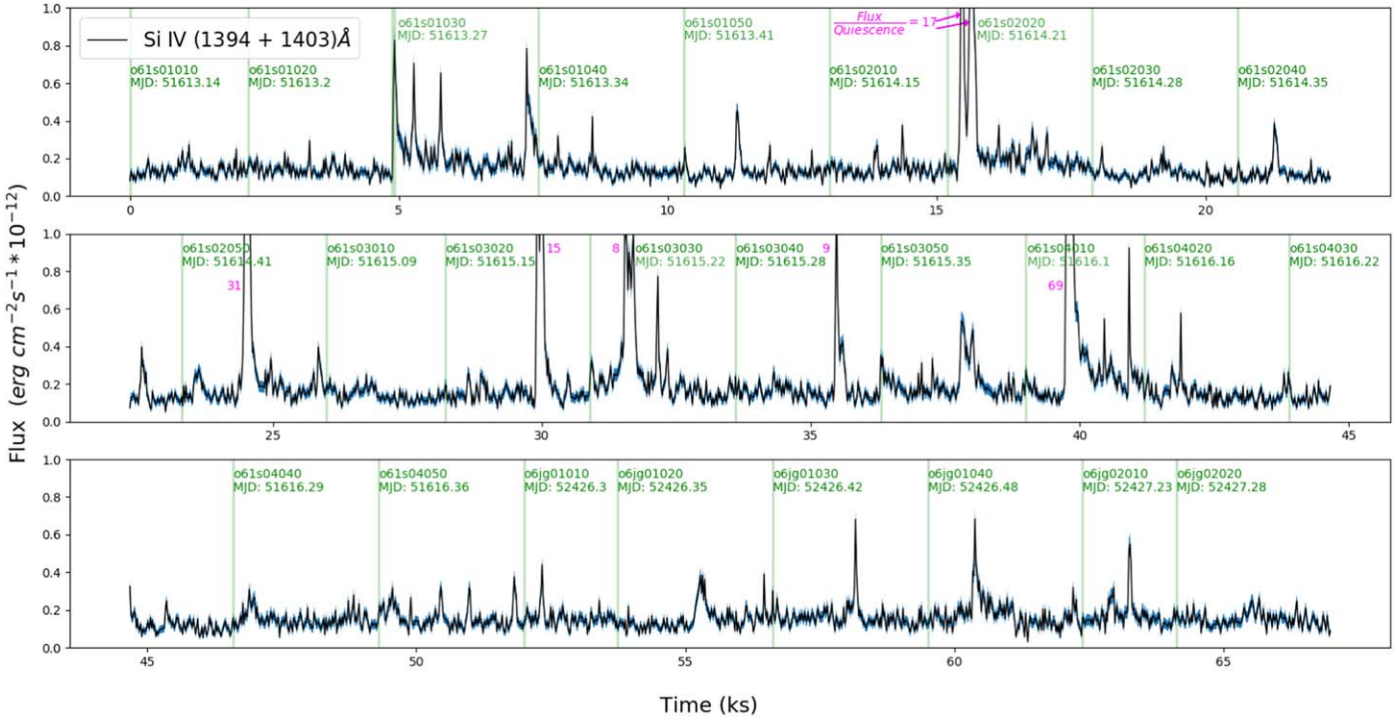

Figure 1. S IV light curve of all STIS E140M observations of AD Leo ($\Delta t = 20$ s, 18.6 hr total). The *y*-axis is flux, and the *x*-axis is time. While time is shown as continuous, each vertical green line represents a gap in time—sometimes years in length. The vertical green text displays the HST ID and the start Modified Julian Date (MJD) of each observation. Overlaid pink numbers are approximate flux-to-quiescence ratios for the peaks of the larger flare events. This figure visually demonstrates the frequency of FUV flares on active M dwarfs and is one of the templates used for hypothetical WTTS flare stars in this study.

Hya, RECX-11, and GM Aur). We then analyze existing archival FUV observations of these three CTTS, as well as new observations of TW Hya obtained by the UV Legacy Library of Young Stars as Essential Standards (ULLYSES; Roman-Duval et al. 2020). We search these observational data for FUV flares and compare the number of flares found against what is predicted. With this method we are testing the accretion masking hypothesis while assuming the null to the decreased flare frequency hypothesis.

In Section 2, we detail the different data products and the sample selection used in this study. In Section 3, we outline our methodology for computing estimated flare rates, FUV flare detectability, flare observations, and the contribution of FUV flares and accretion to the total FUV energy budget of CTTSs. In Section 3.4, we discuss our complementary optical analysis using Transiting Exoplanet Survey Satellite (TESS) data. In Section 4, we report all of the results of this study, and in Section 5, we discuss their implications.

2. Data Products and Sample Selection

2.1. Instrument and Line Selection

The FUV analysis in this study utilizes three atomic ion electric dipole transitions: Si IV at 1394 + 1403 Å, C IV at 1548 + 1551 Å, and He II at 1640 Å. Si IV and C IV are both well known to have strong flare signals, and some flares are also known to have measurable signals in He II (Hawley et al. 2003). In CTTS spectra, the Si IV line can be polluted by H_2 (Herczeg et al. 2002), so corroborating detections in C IV are more convincing evidence of a stellar origin. To numerically compute the flux in the Si IV doublet, C IV doublet, and He II multiplet, the following bounds are used: 1393 Å $< \lambda <$ 1395 Å and 1402 Å $< \lambda <$ 1404 Å (S IV), 1547.6 Å $< \lambda <$ 1551.5 Å (C IV), and 1639.6 Å $< \lambda <$ 1641.5 Å (He II).

The HST Space Telescope Imaging Spectrograph (STIS) and the HST Cosmic Origins Spectrograph (COS) archives are the primary sources of data used in this analysis. AD Leo has been extensively observed (67 ks) with the STIS E140M grating (Loyd et al. 2018b; Loyd & France 2014; Hawley et al. 2003). The E140M grating provides echelle spectra from 1144 to 1710 Å, which contains all three ionic lines used in this study (S IV, C IV, He II). These spectra land on the Multianode Microchannel Array (MAMA) detector hosting a high-resolution format of 2048 × 2048 pixels (Woodgate et al. 1998). The data used in this study were collected in time-tag mode, which includes photon timing information that we use to generate our light curves.

The majority of WTTS and CTTS observations incorporated in this study use COS G160M, though GM Aur is also observed with STIS G140L (Espaillat et al. 2019). All HST data presented in this paper were obtained from the Mikulski Archive for Space Telescopes at the Space Telescope Science Institute. The specific observations analyzed can be accessed via DOI: https://doi.org/10.17909/79br-s977. The bandpass associated with each COS grating is dependent on how the instrument is configured via a cenwave designation. The central wavelength (hereafter: cenwave) denotes the wavelength that approximately falls on the gap between detector segments (Fox et al. 2019). When a cenwave of 1577 Å is used, the instrument will yield an effective bandpass of 1382–1747 Å (with a 20 Å gap in the middle), which contains all three ionic lines used. However, when a higher cenwave is selected, the lower cutoff can be at or above 1394 Å, causing the Si IV line to fall off of the detector and become unavailable. For example, cenwave settings of 1589 and 1611 Å, which are used in the COS

observations of GM Aur, yield minimum wavelengths of 1410 and 1431 Å, respectively. This manifests in Si IV data being observed for less time on each CTTS (Table 2).

2.2. Stellar Sample

In this study, we look at CTTSs and WTTSs, which formed together in nearby SFRs. We pick three stellar pairs to be the targets for this pilot study: TWA-7/TWA Hya from the TW Hydrae Association, RECX-1/RECX-11 from the η Chamaeleontis SFR, and LkCa19/GM Aur from the Taurus-Auriga SFR. Due to their similar formation histories, we assume that the CTTSs and WTTSs that compose each stellar pair have comparable ages and compositions, and we select stars with comparable spectral types. These targets were also chosen because of their close proximity to Earth, as well as their histories of HST observation. Their proximity ($d < 150$ pc) yields FUV data with high signal-to-noise ratios (S/Ns), and their observation histories yield a sizable data archive to comb through. For TW Hya, RECX-11, and GM Aur, there exist roughly 56.7, 6.3, and 10.6 ks, respectively, of G160M/G140L observations.

2.3. Data Products

The Space Telescope Science Institute (STScI) developed and maintains AstroConda, a Python software stack containing many tools for processing and analyzing data products from HST, the James Webb Space Telescope (JWST), and other missions. Among these tools are the HST Calibration Reference Data System (CRDS), stistools, costools, and calcos packages, which can be used to calibrate raw data products and manipulate already-calibrated data products. For this study `CRDS 7.5.0.0`, `stistools 1.3.0`, `costools 3.3.10.dev8+g0c0f43c`, and `calcos 3.3.10.dev8+g0c0f43c` are used.

To conduct our analysis, we needed to create light curves with user-specified time resolutions. First, all COS and STIS observations used are downloaded from the Barbara A. Mikulski Archive for Space Telescopes (MAST). Our process for creating light curves with STIS is as follows: (1) Download the wav.fits (associated wavecal exposure) and tag.fits (time-tag event list) files corresponding to the relevant observations. (2) Run the CRDS procedure to obtain all relevant reference files; if any are missing, they can be located at https://hst-crds.stsci.edu/. (3) Delineate the tag files with stistools.inttag.inttag to produce time-binned outputs with user-specified resolution (20 s). (4) Pass the .inttag output through stistools.calstis.calstis to calibrate the custom binned files, which accounts for a number of parameters, including dead-time fraction. (5) These outputs now contain a number of photon counts at each FUV wavelength (binned every 20 s). The counts in each line are then integrated over the wavelength bounds of that line and converted to flux. To flux-calibrate, we scale the total flux observed in the full x1d exposure file by the ratio of the number of counts observed in each frame to the total number of counts observed over the entire exposure. This yields the flux in each line for every time step of the observation i.e., the time-variable light curve. The method for generating light curves with COS is similar except that the files downloaded are corrtag_a.fits and corrtag_b.fits, costools.splittag.splittag is used instead of stistools.inttag.inttag, and calcos is used instead of calstis.

2.4. Complementary TESS Data

Only one FUV flare was observed across our three CTTS targets at the 5σ confidence level. To verify that our targets are flaring at other wavelengths, we conducted similar stellar pair analysis with optical data. TESS observed the T Tauri stars of this study over 27 days with a cadence of 10 and 30 minutes (Ricker et al. 2014). The specific observations analyzed can be accessed via DOI: https://doi.org/10.17909/ds8a-pz19. To extract and process the associated light curves, we use the TESSExtractor tool (Serna et al. 2021), which uses the TESScut service (Brasseur et al. 2019) to download 10×10 pixel^2 cutouts centered on each target (pixel size $\approx 21''$). An optimal aperture that can vary from 1.0 to 3.5 pixels in radii was selected for each target to perform simple aperture photometry (SAP). The TESS quality flags were considered to reject any anomaly in the photometry (e.g., cosmic rays, popcorn noise, fireworks). Possible contamination of the TESS light curves is estimated using the G-band fluxes of the Gaia-EDR3 sources within the photometric aperture. This contamination is negligible for most of the sample, with a flux contamination of less than 5%. The one exception is GM Aur, which has a brighter companion that could contaminate the photometric aperture (3 pixels of radius), with a target-to-contamination ratio of about 8:5. In this case, we used a smaller photometric aperture of 1 pixel of radius to reduce the contamination from the brighter companion. Finally, since the overall shape of the light curve (including the flares) is recovered using the smaller aperture, we conclude that the detected optical flares belong to GM Aur (see Section 3.4).

3. Methods

3.1. Simulating CTTS Flare Templates

At 4.9 pc away, AD Leo is 10–30 times closer to Earth than the T Tauri stars in this study, and it is among the most well-studied nearby M-type flare stars in the FUV (Hawley et al. 2003; Loyd & France 2014). STIS E140M observations of AD Leo provide an empirical template from which to create hypothetical flaring WTTSs; AD Leo's Si IV light curve is shown in Figure 1 as an example. To create hypothetical WTTS flare light curves, we scale AD Leo's quiescence to the quiescent level of the WTTS for each ion in each stellar pair according to the following scaling factor:

$$S = \frac{F_{q,\mathrm{WTTS}}}{F_{q,\mathrm{ADLeo}}}. \quad (1)$$

These empirical scaling factors for each WTTS are listed in Table 3 in Appendix A. TW Hya is significantly farther away than TWA-7; therefore, we also multiply by a distance correction of $\left(\frac{34\ \mathrm{pc}}{60\ \mathrm{pc}}\right)^2$. These scaling factors yield an AD Leo–like WTTS flare star for each stellar pair. For each WTTS flare template, we subtract the quiescent flux to isolate the hypothetical flare signal. To quantify the associated CTTS's quiescence, we adopt the individual CTTS exposure with the highest rms noise (σ_{CTTS}) in its light curve. Using the highest rms CTTS observation results in a conservative final estimate of the number of flares expected to cross statistical thresholds. To construct the hypothetical flaring CTTS light curve, we then take the sum of the quiescent CTTS light curve and the associated hypothetical WTTS flare template, with their uncertainties added in quadrature. We can then directly

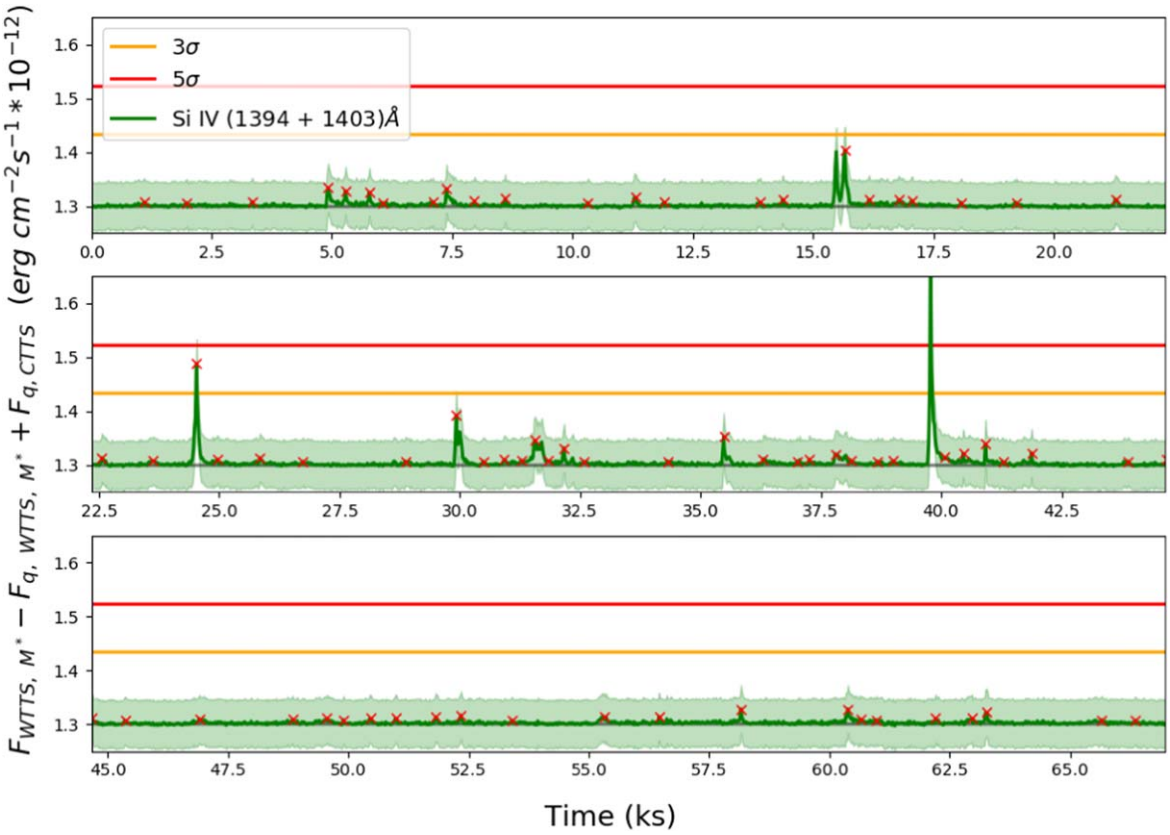

Figure 2. Simulated S IV light curve of TW Hya ($\Delta t = 20$ s, 18.6 hr total). F_{WTTS,M^*} is AD Leo's light curve shown in Figure 1 scaled to TWA-7, and F_{q,WTTS,M^*} is the quiescent flux. $F_{q,\mathrm{CTTS}}$ is the quiescent flux of TW Hya. The y-axis is TWA-7's hypothetical flare signal ($F_{\mathrm{WTTS},M^*} - F_{q,\mathrm{WTTS},M^*}$) added to TW Hya's quiescent flux. The uncertainties in the template fluxes are added in quadrature with the rms of the CTTS quiescent flux—the latter heavily dominates. As a result, the shaded green region effectively represents the 1σ level on the CTTS quiescent flux. The underlying gray line represents the CTTS quiescent flux. The 3σ and 5σ levels are overplotted in orange and red. The result demonstrates how the flare signals, demarcated by red crosses, would penetrate above the CTTS rms noise. This figure indicates that we expect to detect roughly one 5σ and one 3σ flare on TW Hya in 67 ks of observing time.

compare hypothetical CTTS flare signals against the CTTS quiescent level and determine their statistical significance level. This enables us to calculate a lower bound on the number of statistically significant flares that we expect to detect above the CTTS accretion signal. The resulting Si IV light curve for TW Hya can be seen in Figure 2, which is just the light curve from Figure 1 with the aforementioned changes applied.

Overlaid in Figure 2 are the 3σ and 5σ detection levels of the CTTS in orange and red, respectively. The y-axis of this plot is the isolated hypothetical flare signal ($F_{\mathrm{WTTS}} - F_{q,\mathrm{WTTS}}$) added to the quiescent level of the associated CTTS ($F_{q,\mathrm{CTTS}}$), which in this case is TW Hya. This plot is a visual tool that shows how many flares from the template would exceed each of these levels. If, for example, the peak of any given flare signal has an amplitude that is five times greater than the rms variation in the CTTS, then that specific flare would result in a 5σ data point if presented on the CTTS light curve.

We use a time step of 20 s over 67 ks of data, which corresponds to 3350 data points. In a one-sided (positive flare event) normal distribution one would expect a 5σ data point to occur only one time for every 3.5 million data points, i.e., it is highly unlikely that a statistical fluctuation induces a 5σ event within 67 ks. It is clearly seen from the plot in Figure 2 that only a single flare event from the scaled template exceeds the 5σ level. As a note, the undetectable flare at 16 ks would be counted as a single event were it to be detected. This is because both peaks are considered to be within the impulsive range of the flare, which is consistent with how such flares are treated in Loyd et al. (2018b). We would expect to see about five 3σ data points greater than quiescence per 67 ks owing to random Gaussian variation ($(1 - \mathrm{erf}[\frac{3}{\sqrt{2}}]) \times 3350/2 = 4.5$).

Following the methods of Hilton et al. (2011), in order to actually count an event as a flare, we impose the condition that the peak flare signal must be part of three consecutive data points all having a significance of at least 2.5σ. The hypothetical 5σ flare event in Si IV for TW Hya, which can be seen by eye at 39.5 ks in Figure 2, meets this requirement at the measured flux level. The flare at 24 ks does not meet this requirement, though the 5σ level is included within the potential flare's error bars.

To quantify a flare rate from this template, we run a Monte Carlo simulation for 10,000 iterations, allowing each flux data point to vary according to a normal distribution. The measured flux value is taken to be the mean of the distribution, with the extent of the error bars representing the 1σ level. On each iteration, the Hilton criterion is applied and the number of observed flares at the two significance levels is generated. From this simulation, we generate a histogram of observed flare numbers per 67 ks. From these histograms, we reconstruct the mean of the distribution and report errors representing 34.1% of probability space from the mean in both directions so that the combined error region represents an equivalent Gaussian 1σ. Finally, the results are converted from flares per 67 ks to flares per hour (i.e., flare rate).

This analysis is repeated for each of the different ion transitions for each stellar pair, and the results populate the column "Flare Rate (hr^{-1})" in Table 2 (see also the discussion in Section 4). The flare rates are then used to predict the number of flares that may be present in archival light curves by multiplying the rate by the actual amount of time each star has been observed. This result is displayed in the "Flares Expected/Time" column of Table 2. For example, the $0.05^{+0.03}_{-0.03}$ 5σ flares per hour predicted from the light curve in Figure 2 translate to $0.71^{+0.42}_{-0.42}$ flares being predicted in the 14.11 hr that TW Hya is actually be observed.

Our method of stellar pair analysis can be further used to quantify the relative detectability of FUV flares across different stellar pairs. In computing the statistical significance of events (D), we compare the hypothetical WTTS flare signal to the rms flux of the CTTS as follows:

$$D = S * \frac{F_{\mathrm{ADLeo}} - F_{q,\mathrm{ADLeo}}}{\sigma_{\mathrm{CTTS}}} = \frac{F_{\mathrm{ADLeo}} - F_{q,\mathrm{ADLeo}}}{F_{q,\mathrm{ADLeo}}} * \frac{F_{q,\mathrm{WTTS}}}{\sigma_{\mathrm{CTTS}}}. \quad (2)$$

This provides the statistical significance of each data point in units of σ. To assess the relative detectability (D_r) across stellar pairs, we can divide out the common AD Leo–dependent terms $\left(\frac{F_{\mathrm{ADLeo}} - F_{q,\mathrm{ADLeo}}}{F_{q,\mathrm{ADLeo}}}\right)$ and are left with the WTTS quiescent flux divided by the rms about the CTTS flux. In our sample, the WTTS quiescent flux in Si IV only varies by 30%, whereas the CTTS flux rms varies by almost an entire order of magnitude (730%). There is a similar but less pronounced trend in C IV, and the trend is not present in He II. For this limited sample, the rms flux in Si IV of the CTTS itself is a strong indicator of the relative detectability:

$$D_r = \frac{F_{q,\mathrm{WTTS}}}{\sigma_{\mathrm{CTTS}}} \propto \sigma^{-1}_{\mathrm{CTTS}}. \quad (3)$$

In Figure 3, we demonstrate this relationship. We plot the number of expected Si IV flares that cross the 5σ threshold over a period of 10 hr as a function of the CTTS accretion rate; there is no clear correlation between these two parameters. However, we overplot the simplified relative detectability in red and note that it tracks well with the number of predicted flares. Given that the number of flares increases logarithmically as a function of flare energy in standard FFDs (Hilton et al. 2011) and also as a function of peak flux, one would expect a representative sample size to reveal a similar relationship between the number of expected flares and the detectability estimator. This plot demonstrates the predicted results of a 10 hr observing campaign on each of the pilot CTTS targets. Whether or not 10 hr of observation of RECX-11 yields roughly 20 (23.7 predicted) 5σ flares in Si IV would be a good test of the stellar pair analysis technique used in this study and would enable one to distinguish between the accretion masking and decreased flare frequency hypotheses.

By using a WTTS and AD Leo to generate our flare template, we do not consider protostellar outbursts, which may be caused by accretion. If such outbursts exist within the sensitivity realm of this study, then this could cause us to underestimate the number of expected flares. If we observe many more flares than we expect, accretion outbursts are a possible culprit. Another possible faulty assumption is our choice of AD Leo as the archetypal flare star for all three of our stellar pairs. AD Leo may not be the optimal analog for each stellar pair. The general trend is for M dwarfs to be more active at higher masses (Hilton et al. 2011); this would suggest that our sample is potentially more active than AD Leo and could result in further underestimates of the number of expected flares. Lastly, we took the highest rms observation of each CTTS to be its representative value. In reality, there is going to be variation in this parameter, and it will often be lower than the value used in this study. The result of this technique would, again, be a tendency to underestimate the number of predicted flares, though this effect is likely to be negligible because the variation in rms on CTTS is small. All of these assumptions, if faulty, result in our predicted number of flares being less than the observed number.

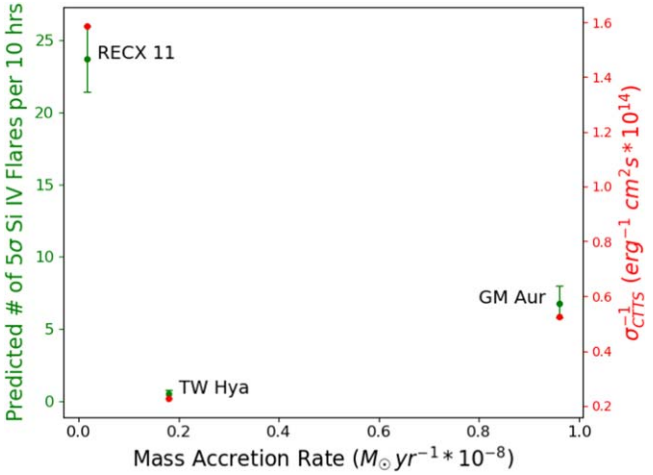

Figure 3. The number of 5σ S IV flares per 67 ks and the simplified relative detectability for each CTTS as a function of accretion rate. The green (left) y-axis shows the number of 5σ S IV flares, and the red y-axis (right) shows the simplified relative detectability, which is just the inverse CTTS flux rms.

3.2. Combing Light Curves for Flares

After estimating the number of flares we expect to have observed, the next step in this process is to examine the CTTS light curves and quantify how many 3σ and 5σ flares are actually observed. To do this, we employ a light-curve-combing algorithm (LCA) that draws on the approaches of Hilton et al. (2011) and Loyd et al. (2018a). Our LCA is an iterative process that independently analyzes different HST observations and searches for potential flares.

The quiescent flux of CTTSs can be constant, slowly increasing, or slowly decreasing. An "increasing" example can easily be seen in C IV at 46 ks (*le9d1el0q*) in Figure 4. The first pass of the LCA quantifies and removes any linear trend in a given exposure. A line is fit to the measured data, and its slope is removed from the observed flux. This can be seen visually in the adjusted light curves in Appendix E. Each figure in Appendix E has a top and a bottom panel; the top panel shows the unadjusted data in black, with the adjusted data in magenta and the fit line in red. The bottom panel shows only the adjusted data. On the second pass, the LCA identifies any data points that are potential flares based on whether the flux is at or greater than two standard deviations away from the mean. Finally, the mean of the observation is calculated, omitting any potential flares, as they would skew the statistic. This mean is taken to be the quiescent flux for that observation, and following Hilton et al. (2011), the precision of the measurement is taken to be the standard deviation. The number of data points

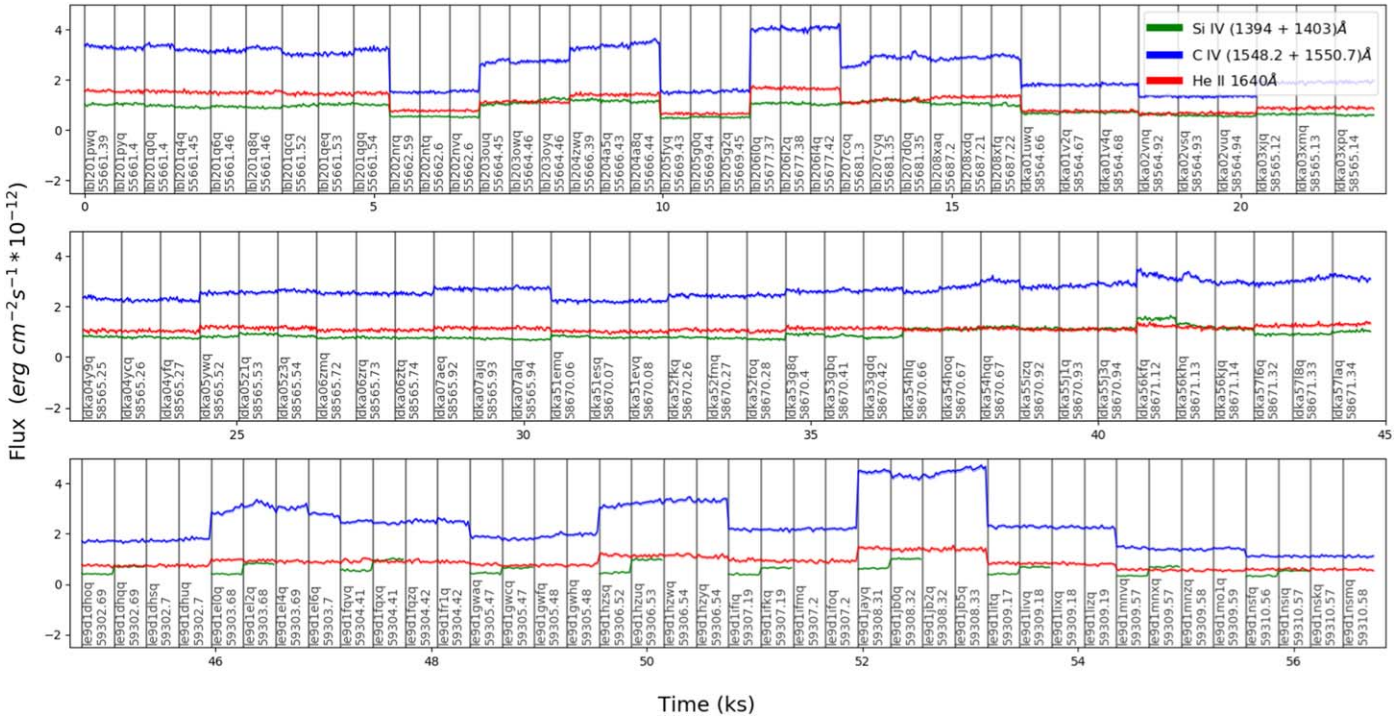

Figure 4. COS G160M light curves of TW Hya for all three ion species ($\Delta t = 20$ s, 15.75 hr total). Vertical black lines signify the beginning of a new observation and a gap in real observation time—sometimes equal to many years. The HST tag and start MJD of each observation are written in black at the bottom of each observation.

Table 1
Stellar Sample Properties

Name	WTTS/CTTS	Spectral Type	Mass ($M_\odot$)	d (pc)	$\dot{M}$ ($M_\odot$ yr^{-1})	Age (yr)
AD Leo	N/A	M3.5	0.4	4.966 ± 0.001	N/A	$(25-300) \times 10^6$ [b]
TW Hydrae	CTTS	K7	0.8	60.09 ± 0.15	1.89×10^{-9}	$(5-10) \times 10^6$ [c]
TWA-7	WTTS	M1	0.5	34.03 ± 0.08	N/A	6.4×10^6 [d]
RECX-11	CTTS	K5	1	98.58 ± 0.25	1.7×10^{-10}	$(5-9) \times 10^6$ [e]
RECX-1	WTTS	K5	0.9	100.16 ± 1.27	N/A	$(5-9) \times 10^6$ [e]
GM Aur	CTTS	K6[a]	0.8	159.64 ± 2.11	9.69×10^{-9}	$(1-10) \times 10^6$ [f]
LkCa19	WTTS	K2[a]	1.3	159.67 ± 2.00	N/A	$(3-16) \times 10^6$ [g]

Note. distances from Gaia data release 2 (Gaia DR2) (Gaia Collaboration 2018). All other data from Ingleby et al. (2013).[a] Herczeg & Hillenbrand (2014)[b] Loyd & France (2014)[c] de la Reza et al. (2006)[d] Binks et al. (2020)[e] Ingleby et al. (2011)[f] Hueso & Guillot (2005)[g] Kraus & Hillenbrand (2009)

that exceed the 3σ and 5σ levels is then calculated. In order for an event to be classified as a flare, we again impose the condition that it must be part of three consecutive points, each having a statistical significance of at least 2.5σ. Across all of our observations, we find one event that breaches the 5σ level with this statistical significance. We describe this flare in detail in Section 4.2. Light curves for other potential flares and a number of selected observations can be found in Appendix E.

To provide the lower bound values, estimated values, and upper bound values of the number of flares observed, the LCA is applied to the archival light curves at the bottoms of their error bars, the measured flux values, and the tops of their error bars, respectively. This method will produce slightly different results than the standard 1σ Gaussian level, effectively due to a rounding of noninteger values to integers. However, this method maintains the occurrence of actual flares as binary events by yielding integer estimations. Results of this method populate the column "Flares Observed" in Table 2 (in Section 4.1) and can be directly compared with the estimated values in the "Flares Expected/Time" column.

3.3. FUV Contributions

In this section, we use a similar Monte Carlo approach to that described in Section 3.1, except now we isolate the contributions from each parameter (WTTSs, CTTSs, and flares) and analyze their variations independently. The France et al. (2014) study of CTTSs, which includes all of the present study's CTTS targets, finds C IV flux to be tightly correlated with FUV emission. Thus, C IV is used as a tracer for the total FUV energy in the present study. We exclude Si IV and He II from this portion of the analysis owing to the propensity of H_2 lines to pollute the Si IV bandpass (Herczeg et al. 2002) and because C IV is a much stronger flare tracer than He II (Hawley et al. 2003). The light curves generated within Monte Carlo iterations are multiplied by $4\pi d^2$ to convert from flux to erg s^{-1}; the distance values used for d can be found in Table 1. These energy-per-time curves for the CTTS quiescence, the WTTS quiescence, and the hypothetical underlying flare signal can then be integrated over the temporal baseline to yield the total energy in C IV contributed from each respective source

Table 2
Results

CTTS	Atomic Lines	Flare Rate (hr^{-1})	Time (hr)	Flares Expected/Time	Flares Observed
TW Hydrae	S IV	3σ:$0.07^{+0.05}_{-0.04}$ 5σ:$0.05^{+0.03}_{-0.03}$	14.11	3σ:$0.99^{+0.71}_{-0.56}$ 5σ:$0.71^{+0.42}_{-0.42}$	3σ:3^{+4}_{-1} 5σ:1^{+1}_{-0}
	C IV	3σ:$0.02^{+0.03}_{-0.02}$ 5σ:$0.01^{+0.02}_{-0.01}$	15.75	3σ:$0.32^{+0.47}_{-0.32}$ 5σ:$0.16^{+0.32}_{-0.16}$	3σ:2^{+2}_{-1} 5σ:1^{+2}_{-1}
	He II	3σ:$0.00^{+0.01}_{-0.00}$ 5σ:$0.00^{+0.00}_{-0.00}$	15.75	3σ:$0.00^{+0.16}_{-0.00}$ 5σ:$0.00^{+0.00}_{-0.00}$	3σ: 05σ: 0
RECX-11	S IV	3σ:$3.19^{+0.29}_{-0.27}$ 5σ:$2.37^{+0.23}_{-0.23}$	0.62	3σ:$1.98^{+0.18}_{-0.17}$ 5σ:$1.47^{+0.14}_{-0.14}$	3σ: 0 5σ: 0
	C IV	3σ:$1.77^{+0.19}_{-0.18}$ 5σ:$1.35^{+0.15}_{-0.14}$	1.76	3σ:$3.12^{+0.33}_{-0.32}$ 5σ:$2.38^{+0.26}_{-0.15}$	3σ: 0 5σ: 0
	He II	3σ:$0.96^{+0.18}_{-0.16}$ 5σ:$0.65^{+0.14}_{-0.12}$	1.76	3σ:$1.69^{+0.32}_{-0.28}$ 5σ:$1.14^{+0.25}_{-0.21}$	3σ: 0 5σ: 0
GM Aur	S IV	3σ:$0.90^{+0.15}_{-0.13}$ 5σ:$0.68^{+0.12}_{-0.10}$	2.62	3σ:$2.36^{+0.39}_{-0.34}$ 5σ:$1.78^{+0.31}_{-0.26}$	3σ:0^{+2}_{-0} 5σ: 0
	C IV	3σ:$0.46^{+0.09}_{-0.08}$ 5σ:$0.37^{+0.06}_{-0.06}$	2.96	3σ:$1.36^{+0.27}_{-0.24}$ 5σ:$1.10^{+0.18}_{-0.18}$	3σ:0^{+1}_{-0} 5σ: 0
	He II	3σ:$0.00^{+0.01}_{-0.00}$ 5σ:$0.00^{+0.01}_{-0.00}$	2.96	3σ:$0.00^{+0.03}_{-0.00}$ 5σ:$0.00^{+0.03}_{-0.00}$	3σ:0^{+3}_{-0} 5σ: 0

Note. A description of the calculation of flare rates and the number of expected flares can be found in Section 3.1. A description of how the actual number of flares observed is calculated can be found in Section 3.2.

($E_{\rm CTTS}$, $E_{\rm WTTS}$, $E_{\rm Flares}$):

$$E_i = 4\pi d^{2*}\int_0^t F_i\, dt, \quad i = \text{CTTS, WTTS, Flares.} \tag{4}$$

With our finite numerical templates, this integral is approximately solved via the composite trapezoidal rule. The distance correction in Equation (4) is not necessary to yield correct percent contributions, but it is necessary to yield absolute energy values. If there are no flares occurring in the underlying CTTS, then the contribution to the total C IV energy from accretion is

$$\text{accretion signal contribution} = \frac{E_{\rm CTTS} - E_{\rm WTTS}}{E_{\rm CTTS}}. \tag{5}$$

Equation (5) represents an upper-limit estimate to the accretion contribution assuming that there are no flares. Alternatively, if the star is flaring with an FFD similar to AD Leo's, then the flare contribution to the total C IV energy is

$$\text{flare contribution} = \frac{E_{\rm FLARE}}{E_{\rm CTTS}}. \tag{6}$$

Our Monte Carlo approach yields a normal distribution for each of these values. Therefore, we treat C IV as a proxy for the total FUV energy and report the mean and standard deviation of the Monte Carlo normal distributions as our results in Section 4.

3.4. Complementary TESS Analysis

While it is well documented that CTTSs flare at nominal levels in the X-ray (Getman & Feigelson 2021), we used TESS archival data to verify that our three CTTS targets also flare in the optical. Light curves for our targets are generated for the TESS bandpass (6000–10000 Å). We then detrend the light curves and compute the normalized flux ($\text{Flux}_{\rm fl}(t)$). The broadband luminosity ($L_{\rm fl}$) and energy ($E_{\rm fl}$) of any observed flare are then calculated as follows:

$$L_{\rm fl}(t) = 4\pi d^2 * (\text{Flux}_{\rm fl} - 1)(t) * F_{\rm cont}, \tag{7}$$

$$E_{\rm fl} = \sum L_{\rm fl}(t) * \Delta T_{\rm LC}, \tag{8}$$

where d is the distance to the star in cm and $F_{\rm cont} = F_{{\rm ZP}_T} \cdot 10^{(-0.4 \cdot m_{T_o})}$ is the continuum flux, based on the dereddened TESS magnitude of the star (m_{T_o}). We used the extinction in the TESS band $A_T = 2.06 \cdot E(B-V)$ (Stassun et al. 2019) and the zero-point flux $F_{{\rm ZP}_T} = 1.34093 \times 10^{-9}$ erg cm^{-2} s Å (Rodrigo & Solano 2020; Rodrigo et al. 2012). As a result, the median luminosity for all stars is 3.6×10^{32} erg s^{-1} ($0.094\, L_\odot$). We calculate flare energy as the summation of the luminosity in each time interval multiplied by the light-curve cadence ($\Delta T_{\rm LC}$), corresponding to 600 s or 1800 s. Tables 4(A) and (B) in Appendix B summarize the information of the detected flares. The types of flares are classified as normal (n) or microflare (m) and as having symmetrical (s) or asymmetrical profiles (a). Microflares are understood as signals that have at least three consecutive points over 1.5σ (as opposed to 2.5σ). The moment when the flare begins ($T_{\rm in}$) is listed in barycentric Julian days (BJD). Lastly, we compare the maximum flux of each observed flare with the highest associated CTTS rms flux and open the question as to whether accretion masking may also be occurring at optical wavelengths.

4. Results

4.1. Flare Numbers

We have computed the number of statistically significant flares we expect to see per hour and extrapolated this rate to produce the number expected for the actual time observed according to the procedure laid out in Section 3.1. These two values are shown in Table 2 in the columns "Flare Rate (hr^{-1})" and "Flares Expected/Time," respectively. The "Time (hr)" column shows the number of hours each target was actually observed. We then apply our LCA, as described in Section 3.2, to the HST light curves to yield the number of flares actually observed. This value is reported in Table 2 in the column "Flares Observed." We also apply the LCA in search of statistically significant negative events, which can represent absorptive astrophysical phenomena crossing our line of sight (Kiefer et al. 2014), but none are observed.

We find general agreement between the predicted and observed number of flares at the 5σ level, as well as some agreement at the 3σ level, but these results are in the realm of small number statistics. We find less than the number of expected flares on RECX-11, though it is possible that the number of observed flares will approach the number of estimated flares as we increase the observation time. In order

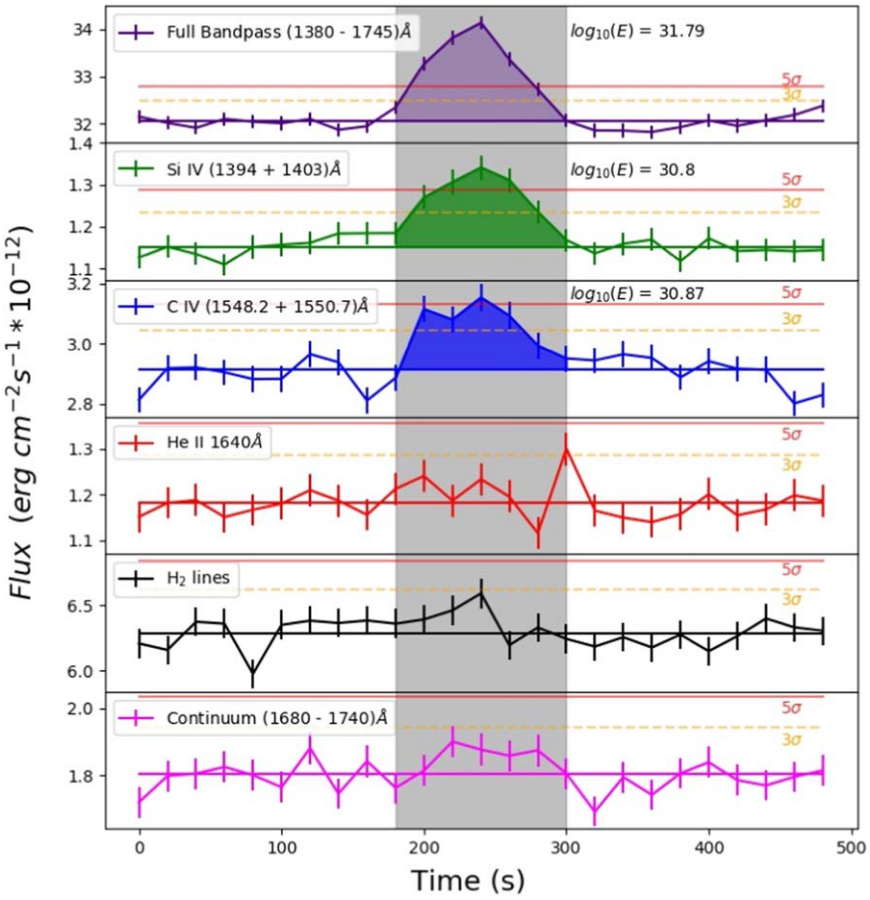

Figure 5. The first FUV flare on a CTTS (TW Hya, $\Delta t = 20$ s). The gray shaded region is the manually identified temporal extent of the flare. A nondetection in accretion-associated continuum and in H_2 lines suggests a likely stellar origin. Both S IV and C IV show statistically significant flares at the 5σ level.

to raise the number of estimated flares so that they are significantly different from 0 and 1, we require longer-duration observations of the CTTS, and the amount of time required is different for each stellar pair.

4.2. Flares on TW Hya

Across all applications of the LCA to CTTSs, we identify two flares that meet our criteria (described in Section 3) for statistical significance: one of them a $>5\sigma$ event in C IV (7σ in Si IV), and the other a $>3\sigma$ event in C IV (4.8σ in Si IV). Both were observed on TW Hya and can be found in HST ID observations *lbl207d0q* and *lbl208xfq*, respectively. The $>5\sigma$ event is also, by definition, a $>3\sigma$ event. The event that is $>3\sigma$ but $<5\sigma$ (*lbl208xfq*) is only statistically significant in Si IV. There are also two other potential $>3\sigma$ events (i.e., error bars breach $>3\sigma$ level) that are both in C IV (*ldka56khq*, *le9d1e2q*). There is no corresponding signal in Si IV or He II for either of these potential events. Light curves for these potential flares, as well as a number of other light curves for each CTTS, can be found in Figures 9, 10, and 11 in Appendix E.

In Figure 5, we present the first definitive FUV flare observed on a CTTS. The flare (*lbl207d0q*) is a statistically significant event at 7σ in Si IV and 6σ in C IV. There is no significant flare signal observed in He II. The LCA identified the existence of the flare region, whereas the temporal extents of the flare are manually selected. Light curves of the flare in H_2 and continuum emission 1680–1740 Å related to accretion are also created. The lines used to compute the H_2 light curve in Figure 5 are centered at 1446, 1453, 1463, 1489, 1500, and 1505 Å and are excited by the core of the Lyα line, which itself may participate in the flare event. H_2 and and the continuum are only marginally elevated during this time period, suggesting a stellar origin. During the flare, the S IV and C IV fluxes are enhanced by 16% and 9%, respectively, whereas the H_2 and continuum lines both see a roughly 5% increase. Integrating the flare signal (flux–quiescence) over the time period of the flare (shaded gray region in Figure 5) and multiplying by $4\pi d^2$ yields the total energy released in the flare at the star. We find total energies in Si IV and C IV to be $(6 \pm 1) \times 10^{30}$ erg and $(7 \pm 2) \times 10^{30}$ erg, respectively. For the entire bandpass (1380–1745 Å), we find an energy of $(6.1 \pm 0.7) \times 10^{31}$ erg. We also compute the equivalent duration (Gershberg 1972) of the flare in the entire bandpass to be 4.4 ± 0.5 s. For context, FUV flares on M dwarfs with an equivalent duration of $10\,\mathrm{s} < \delta < 1000\,\mathrm{s}$ are classified as frequent but often undetectable (Loyd et al. 2018a).

4.3. RECX-1 Flare

In the course of our light-curve creation, we analyzed archival spectra of the K5 WTTS RECX-1. The very broad wings of the Si IV lines in the COS G130M spectra of RECX-1 indicated an additional chromospheric energy input. Subsequent analysis of the FUV light curve of RECX-1 revealed the first detection of an FUV flare on a WTTS. This flare was observed with COS G130M. G130M has an upper spectral limit of 1470 Å, which only contains one of the three lines (Si IV) incorporated in this

project, and thus was not part of our original study. The FUV flare on RECX-1, shown in Figure 7 in Appendix C, is the most energetic flare event ever observed in the FUV with either COS or STIS. We find a total energy in the FUV bandpass (1135–1429 Å) of $(2.1 \pm 0.1) \times 10^{32}$ erg, which is 59%–75% larger than the energetic flare observed on a 40 Myr M star (GSC 8056–0482) at 1.26×10^{32} erg (Loyd et al. 2018b). We compute the flare to have an equivalent duration of 957 ± 66 s. We do not make any corrections for interstellar dust reddening ($A_v = 0$; Luhman & Steeghs 2004). If we adopt the small but nonzero interstellar reddening curve suggested by the line-of-sight H I analysis of McJunkin et al. (2014), the total energy would be about 10% higher. We also exclude Lyα and O I from the analysis owing to geocoronal contamination. It is possible that the flare on RECX-1 is a superflare, meaning that the total bolometric energy of the flare signal exceeds 10^{33} erg. While it is a strong FUV event, it is not associated with strong increases in the continuum or in Fe XXI, so we do not expect it to be associated with an intense X-ray flare. We note in passing that the CTTS and WTTS flares in this study do not exhibit the classical temporal flare profile. Flare profiles are typically described by an instantaneous rise, which leads to an impulsive range that is followed by an exponential decay (Loyd et al. 2018a), but we also note that X-ray flares of PMS stars also sometimes deviate from the canonical shape with more gradual rise and decay phases (see examples in Getman & Feigelson 2021; Getman et al. 2021). These studies find a handful of flares with rise times roughly equal to decay times, similar to what is found in the present study. In the X-ray, these must be genuinely magnetic events, as no accretion contribution is present at the photon energies where the flares are observed.

4.4. Flare Analysis with Full FUV Bandpass

In the analysis of the CTTS and WTTS flares, it is apparent that the full bandpass light curves provide the highest S/N. This is because the entire bandpass contains an order of magnitude more photons per time step than the individual strong lines. This is one reason why previous studies used the entire available FUV bandpass to identify flares in the light curves of M stars (Loyd et al. 2018a; France et al. 2020). In our case, the majority of this additional flux is attributable to the underlying FUV continuum, other lower ionization lines, and 200+ molecular hydrogen lines (Herczeg et al. 2002). To take advantage of this increased sensitivity, we created as large a bandpass as possible to compare the same spectral region across the STIS E140M and COS G160M gratings for our stellar pair analysis (1439–1561 Å + 1635–1700 Å). The light curve for this bandpass on TW Hya is shown in Figure 8 in Appendix D. The first CTTS flare we observed from the light-curve analysis of strong lines is encircled in magenta. This flare occurs in the middle of its observation window and has a relatively well behaved quiescent flux. We are able to observe this flare with greater statistical significance (14σ) than with the strong-line light curves (7σ in Si IV). Additionally, a number of potential flares and other interesting activity are revealed, encircled in red and green, respectively. However, the combination of increased sensitivity, in addition to a significant H_2 component, results in a more dynamic light curve that has greater resolved variability and temporal trends with increasing or decreasing flux for many of the frames. These dynamic features in the light curve are large compared to the uncertainty in the flux. Therefore, we believe that the observed time variability is real (e.g., *ldka55izq* and *ldka56kfq*) as opposed to being manifest

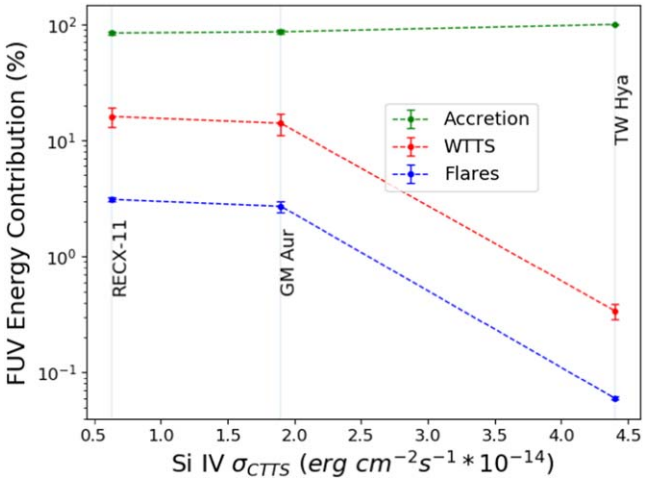

Figure 6. Contributions to the total FUV energy budget from accretion, the underlying WTTS, and flares are shown for each of the three CTTS targets. Percentages are calculated from Monte Carlo–generated normal distributions.

Gaussian noise about the quiescent flux level. For most of the frames with potential flares and significant variability, we are unable to establish the quiescent flux level with confidence. The single exception is the flare already identified by the LCA in Si IV and C IV in Section 4.2. Therefore, band-integrated light curves on CTTSs do not present a significant improvement in flare finding owing to H_2 contamination and to the difficulty in establishing the quiescent flux level. However, properly adding the hot accretion line light curves together, without the rest of the continuum, could increase the S/N and be a better option for future studies.

4.5. Flare and Accretion Contributions to FUV Energy Budget

We compute upper limits on the accretion contribution to the total FUV energy for each CTTS. Using Equation (5) in Section 3.3, we find these limits to be $99.66\% \pm 0.05\%$, $84\% \pm 3\%$, and $86\% \pm 3\%$ for Tw Hya, RECX-11, and GM Aur, respectively. If flaring with an FFD similar to AD Leo, we estimate the flare contributions to the total FUV energy (Equation (6)) to be $0.064\% \pm 0.002\%$, $3.1\% \pm 0.1\%$, and $2.7\% \pm 0.3\%$ for TW Hya, RECX-11, and GM Aur, respectively. To estimate a lower limit on the accretion contribution given the AD Leo paradigm, one can subtract the comparatively small flare contributions. We also compute the contribution from the underlying WTTS. These results are plotted in Figure 6. While RECX-11 and RECX-1 are of the same spectral type, the WTTS partners for TW Hya and GM Aur are spectrally mismatched (see Table 1); this will lead to us overestimating the accretion contribution on TW Hya and underestimating the contribution on GM Aur. However, we used the best WTTSs for which there exist observations, and the resultant accretion contributions are consistent with predictions using a power-law fit to observational data (see Figure 4 in Ardila et al. 2013).

4.6. TESS Analysis

We detected a total of 52 flares over 3.5 hr in available TESS data across all of the CTTS and WTTS targets, with TWA-7 and RECX-1 contributing most of the detected flares. The vast majority of observed flares exhibit the traditional asymmetrical flare profile (sharp rise with exponential decay). Two examples are shown in Figure 12 in Appendix F: one from TW Hya and

one from RECX-11. We find an average flare energy of 6.48×10^{35} erg across all observed flares, which is higher than that reported for nearby main-sequence stars (e.g., M dwarfs, Günther et al. 2020; G-type dwarfs, Shibayama et al. 2013). However, higher average flare energies in younger stellar populations are consistent with what is observed in other optical (Ilin et al. 2021) and X-ray (Getman & Feigelson 2021) studies, and we may not be sensitive to lower-energy flares owing to the distance of our targets (Jackman et al. 2019). Tables 4(A) and (B) in Appendix B summarize the information of the detected flares. The shape of the flares found were mostly typical with fast growth and slower decay, making them asymmetric. However, in five instances, the rise time was found to be similar to the fall time, so the shape was roughly symmetric. The average duration of flares is 2.5 hr. We find that CTTSs in this complementary analysis consistently demonstrate lower flare rates than their WTTS partners, though a more comprehensive study would be required to determine whether this trend persists beyond our sample. TWA-7 and RECX-1 flare about three times as often as TW Hya and RECX-11, respectively, and LkCa19 flares twice as often as GM Aur. We also find that the vast majority of optical WTTS flares would not be observable, or would be difficult to observe, above the associated CTTS rms noise. When taken together with our finding that WTTS flare rates appear to be higher, this suggests that accretion masking might also be occurring in the TESS bandpass. This is an interesting possibility to probe for future studies, but the current analysis sufficiently demonstrates that our targets are flaring in the optical, which was the goal of this complementary analysis. This dispels the possibility that we do not observe flares on our CTTSs in the FUV because they are not flaring.

5. Discussion and Conclusions

We set out with the question, "Given their prevalence on even inactive M dwarfs, why do we not see frequent FUV flares in HST observations of late-type accreting protostars?" The answer could have meaningful implications on protoplanetary disk dispersal and improve our understanding of the physical mechanisms behind stellar flares. To probe this question, we employed the WTTS/CTTS stellar pair analysis described in Section 3, which invokes a number of assumptions further described at the end of Section 3.1. These assumptions include using AD Leo and a WTTS to generate each flare template and using the noisiest CTTS rms observation as the representative value to compare hypothetical flares against. Each of the assumptions discussed could lead to fewer flares being predicted than observed. Given that the number of expected flares is not smaller than the number of observed flares, we do not consider the effects of these assumptions to be significant.

This pilot study reveals the lack of flares observed in the FUV on CTTSs and demonstrates the empirical technique of WTTS/CTTS pair analysis in order to probe this quandary. While we did observe an FUV flare on a CTTS and a WTTS, the results of this study are unable to reject either of the hypotheses proposed to explain why we do not see frequent FUV flares in HST observations of late-type accreting protostars. Our stellar pair analysis, which tests accretion masking, predicts that we would observe $23.7^{+2.3}_{-2.3}$ 5σ flares in Si IV on RECX-11 over 10 hr. This is the best prediction from our study given the proper spectral match between RECX-1 and RECX-11. Such an observing campaign would be able to differentiate between the two hypotheses, except in the scenario in which actual flare frequencies are coincidentally decreased by the same proportion predicted from accretion masking. Our TESS analysis suggests that the targets are flaring within nominally expected rates in the optical, which lends credence to the possibility that they are also flaring in the FUV, but that the flare signals are being masked under accretion luminosity. We also find consistently higher flare rates among the WTTSs when compared to the CTTSs in the TESS data, which is evidence that some level of masking may also be occurring at optical wavelengths. The results of the current study suggest the following:

1. Accretion masking remains a valid hypothesis to explain the lack of observed FUV flares on CTTSs and may also be operating at optical wavelengths.
2. The accretion contribution to the total FUV energy budget dominates over the underlying quiescent and flare contributions from stellar magnetic activity.
3. The rms variation about the quiescent flux of CTTSs can be used as a tool to predict the relative detectability of FUV flares.

These results imply that FUV flares are not likely to be an important contributor to photoevaporative winds and planetary disk dispersal. This is because, for the targets in this study, the FUV contribution from accretion far outweighs any potential flare component, and FUV flares are relatively rare events. X-ray flares, on the other hand, may yet be a significant contributor to the disks' wind-driven mass loss (Getman & Feigelson 2021).

We plan to extend this pilot study to the entire HST-COS archive of WTTSs/CTTSs in order to better constrain the results found here and to expand the reservoir of data on CTTSs through monitoring observations acquired by ULLYSES (Roman-Duval et al. 2020). The ULLYSES monitoring campaign will observe both TW Hya and GM Aur for 24 orbits over the next 12 months, in addition to the other well-studied CTTSs RU Lup and BP Tau. This will represent a major increase in the time available for flare searches on archetypal, accreting protostars. Future work involves analyzing these monitoring observations for flares and extending the stellar mass and mass accretion rate parameter space probed with WTTS/CTTS stellar pair analysis.

The authors extend thanks to Nicholas Kruczek, Arika Egan, Nils Halverson, Isaiah Tristan, and Fernando Cruz Aguirre for useful conversations. Support for program No. HST-AR-16129.025 (P.C.H. and K.F.) and No. HST-GO-15204.001 (H.M.G.) was provided by NASA through grants from the Space Telescope Science Institute (STScI), which is operated by the Associations of Universities for Research in Astronomy, Incorporated, under NASA contract NAS5-26555. J.H., M.G. B., and J.S. acknowledge support from CONACyT project No. 86372 and the UNAM-PAPIIT project IA102921. This work is based on observations obtained with the NASA/ESA Hubble Space Telescope, retrieved from the Mikulski Archive for Space Telescopes (MAST), which is maintained by STScI. This paper includes data collected with the Transiting Exoplanet Survey Satellite (TESS) mission, also obtained from MAST/STScI. Funding for the TESS mission is provided by the NASA Explorer Program. Lastly, this work greatly benefited from discussions with the ODYSSEUS team (HST AR-16129), https://sites.bu.edu/odysseus/ (Espaillat et al. 2022).

Appendix A
AD Leo Scaling Factors

Table 3
Ion-dependent Scaling Factors

Name	S IV	C IV	He II
TWA-7	0.17 ± 0.06	0.09 ± 0.01	0.14 ± 0.02
RECX-1	0.14 ± 0.04	0.10 ± 0.01	0.13 ± 0.02
LkCa19	0.18 ± 0.06	0.051 ± 0.009	0.05 ± 0.01

Note. These are the scaling factors required to simulate hypothetical WTTS flare stars from AD Leo templates. These factors are the quiescent flux of the WTTS divided by the quiescent flux of AD Leo for each ion.

Appendix B
TESS Flare Data

Table 4
Optical Flare Data

Object	ID	Type	$\Delta T_{\rm LC}$ (hr)	$\#{\rm Fl}/\Delta T_{\rm LC}$ (#/hr)	$\overline{\#Fl/\Delta T_{\rm LC}}$ (#/hr)	$T_{\rm in}$ (BJD)	ΔT (hr)	T_r (hr)	$T_{\rm dc}$ (hr)	Fl. Flux $/\sigma$	$L_{\rm fl}$ (erg s^{-1})	$E_{\rm fl}$ (erg)
						A						
GM Aur	1-1	n,a	563.493	0.0035	0.0037	1817.6830	7.50	3.50	4.00	4.36	4.32E+32	7.78E+35
	1-2	n,s				1836.6620	3.00	1.50	1.50	6.69	6.92E+32	1.24E+36
	2-1	m,a	528.213	0.0038		2480.7694	1.50	0.67	0.83	2.76	8.22E+31	4.93E+34
	2-2	n,a				2488.5548	1.00	0.33	0.67	4.26	1.42E+32	8.51E+34
LkCa19	2-1	n,a	528.213	0.0076	0.0076	2474.2966	2.17	0.50	1.67	45.81	4.93E+33	2.96E+36
	2-2	n,s				2477.4566	2.33	0.83	1.50	5.45	6.43E+32	3.86E+35
	2-3	n,a				2478.9706	1.17	0.33	0.83	5.28	2.67E+32	1.60E+35
	2-4	n,a				2480.9083	1.17	0.17	1.00	3.66	1.80E+32	1.08E+35
RECX-11	1-1	m,a	1264.000	0.0016	0.0011	1620.8877	7.00	2.00	5.00	2.99	3.63E+33	6.54E+36
	1-2	n,s				1650.9916	7.50	3.50	4.00	9.30	8.45E+33	1.52E+37
	2-1	n,a	1841.339	0.0005		2315.6234	2.00	0.33	1.67	299.21	5.39E+33	3.24E+36
RECX-1	1-1	n,a	1263.000	0.0063	0.0054	1605.9918	2.00	0.50	1.50	0.44	4.52E+32	8.14E+35
	1-2	n,a				1610.9085	2.50	0.50	2.00	0.52	4.08E+32	7.34E+35
	1-3	n,a				1615.4085	3.00	1.00	2.00	0.32	4.40E+32	7.93E+35
	1-4	n,s				1620.7419	3.50	1.00	2.50	0.12	3.08E+32	5.55E+35
	1-5	n,a				1630.5127	3.00	0.50	2.50	0.18	2.67E+32	4.80E+35
	1-6	n,a				1636.0543	4.00	1.00	3.00	0.18	1.89E+32	3.41E+35
	1-7	n,a				1643.3251	3.50	1.00	2.50	0.23	3.13E+32	5.64E+35
	1-8	n,s				1651.2208	2.00	1.00	1.00	0.13	1.87E+32	3.37E+35
	2-1	n,a	1841.339	0.0049		2312.8803	1.50	0.33	1.17	0.39	2.27E+32	1.36E+35
	2-2	n,a				2313.7970	1.83	0.50	1.33	0.47	4.18E+32	2.51E+35
	2-3	n,a				2323.0888	1.50	0.17	1.33	0.90	5.92E+32	3.55E+35
	2-4	n,a				2330.4916	1.17	0.33	0.83	0.29	1.82E+32	1.09E+35
	2-5	n,a				2339.9289	0.83	0.33	0.50	0.31	1.08E+32	6.50E+34
	2-6	n,a				2340.3108	2.00	0.67	1.33	0.50	5.01E+32	3.00E+35
	2-7	n,a				2359.2485	1.33	0.33	1.00	0.28	2.30E+32	1.38E+35
	2-8	n,a				2377.8248	2.17	0.50	1.67	0.30	2.92E+32	1.75E+35
	2-9	n,a				2385.5886	1.50	0.33	1.17	0.26	2.24E+32	1.34E+35
	3-1	n,a	604.507	0.0050		1585.9491	3.00	1.00	2.00	1.38	1.69E+33	3.05E+36
	3-2	n,a				1591.2199	2.00	0.50	1.50	0.35	3.60E+32	6.49E+35
	3-3	n,a				1594.5741	2.50	0.50	2.00	0.17	1.89E+32	3.40E+35

Table 4
(Continued)

Object	ID	Type	$\Delta T_{\rm LC}$ (hr)	$\#{\rm Fl}/\Delta T_{\rm LC}$ (#/hr)	$\overline{\#Fl/\Delta T_{\rm LC}}$ (#/hr)	$T_{\rm in}$ (BJD)	ΔT (hr)	T_r (hr)	$T_{\rm dc}$ (hr)	Fl. Flux $/\sigma$	$L_{\rm fl}$ (erg s^{-1})	$E_{\rm fl}$ (erg)
					B							
TW Hydrae	1-1	n,a	579.174	0.0052	0.0052	2294.0639	1.83	0.17	1.67	11.28	4.04E+32	2.42E+35
	1-2	n,s				2296.8903	2.50	1.00	1.50	15.74	9.07E+32	5.44E+35
	1-3	n,a				2301.9875	2.00	0.33	1.67	14.08	8.85E+32	5.31E+35
TWA-7	1-1	n,a	578.328	0.0225	0.0186	2283.8695	0.83	0.17	0.67	1.30	6.26E+30	3.76E+33
	1-2	n,a				2283.9459	2.00	0.17	1.83	1.99	2.45E+31	1.47E+34
	1-3	n,a				2287.8973	1.83	0.33	1.50	2.84	3.91E+31	2.34E+34
	1-4	m,a				2289.2862	1.17	0.33	0.83	2.09	1.07E+31	6.40E+33
	1-5	n,a				2289.8486	1.83	0.17	1.67	17.41	2.03E+32	1.22E+35
	1-6	n,a				2290.6473	1.33	0.33	1.00	3.67	2.49E+31	1.50E+34
	1-7	n,a				2290.8139	1.00	0.17	0.83	3.04	1.91E+31	1.15E+34
	1-8	n,a				2295.6541	1.83	0.33	1.50	2.46	3.54E+31	2.12E+34
	1-9	n,a				2295.9319	1.33	0.17	1.17	2.60	2.13E+31	1.28E+34
	1-10	n,a				2297.2652	1.50	0.17	1.33	8.73	4.61E+31	2.77E+34
	1-11	n,a				2297.3902	1.33	0.33	1.00	3.38	2.17E+31	1.30E+34
	1-12	n,a				2297.8763	1.83	0.33	1.50	11.64	1.34E+32	8.04E+34
	1-13	n,a				2301.0360	1.00	0.17	0.83	2.46	1.47E+31	8.81E+33
	2-1	n,a	544.007	0.0147		1544.3903	2.00	0.50	1.50	1.83	2.77E+31	4.98E+34
	2-2	n,a				1553.6614	4.00	1.00	3.00	4.10	7.44E+31	1.34E+35
	2-3	n,a				1557.7031	6.00	1.00	5.00	6.79	1.23E+32	2.21E+35
	2-4	n,a				1560.8698	3.00	0.50	2.50	6.36	8.54E+31	1.54E+35
	2-5	n,a				1560.9948	4.00	1.50	2.50	2.79	6.75E+31	1.22E+35
	2-6	m,a				1562.6198	3.00	0.50	2.50	1.05	1.52E+31	2.73E+34
	2-7	n,a				1562.8489	3.00	1.00	2.00	1.14	1.80E+31	3.25E+34
	2-8	n,a				1566.5989	4.00	1.00	3.00	1.53	3.82E+31	6.87E+34

Note. The ID combines the epoch of each observation and the chronological order in which each flare is observed. The types of flares were classified into normal (n) or microflares (m) and symmetrical (s) or asymmetrical profiles (a). $\Delta T_{\rm LC}$ is the time span of the light curve. $\#{\rm Fl}/\Delta T_{\rm LC}$ is rate of flares, and $\overline{\#{\rm Fl}/\Delta T_{\rm LC}}$ is its average. The moment when the flare begins ($T_{\rm in}$) is listed in barycentric Julian days (BJD). The rise time (T_r), decay time ($T_{\rm dc}$), and total duration of the flare (ΔT) are listed in hours. Fl. Flux$/\sigma$ is the peak flare flux (after subtracting quiescence) divided by the associated CTTS rms. Lastly, $L_{\rm fl}$ and $E_{\rm fl}$ are the luminosity and energy of the flare, respectively. The specific TESS observations analyzed can be accessed via DOI: https://doi.org/10.17909/ds8a-pz19.

Appendix C
RECX-1 (WTTS) Flare

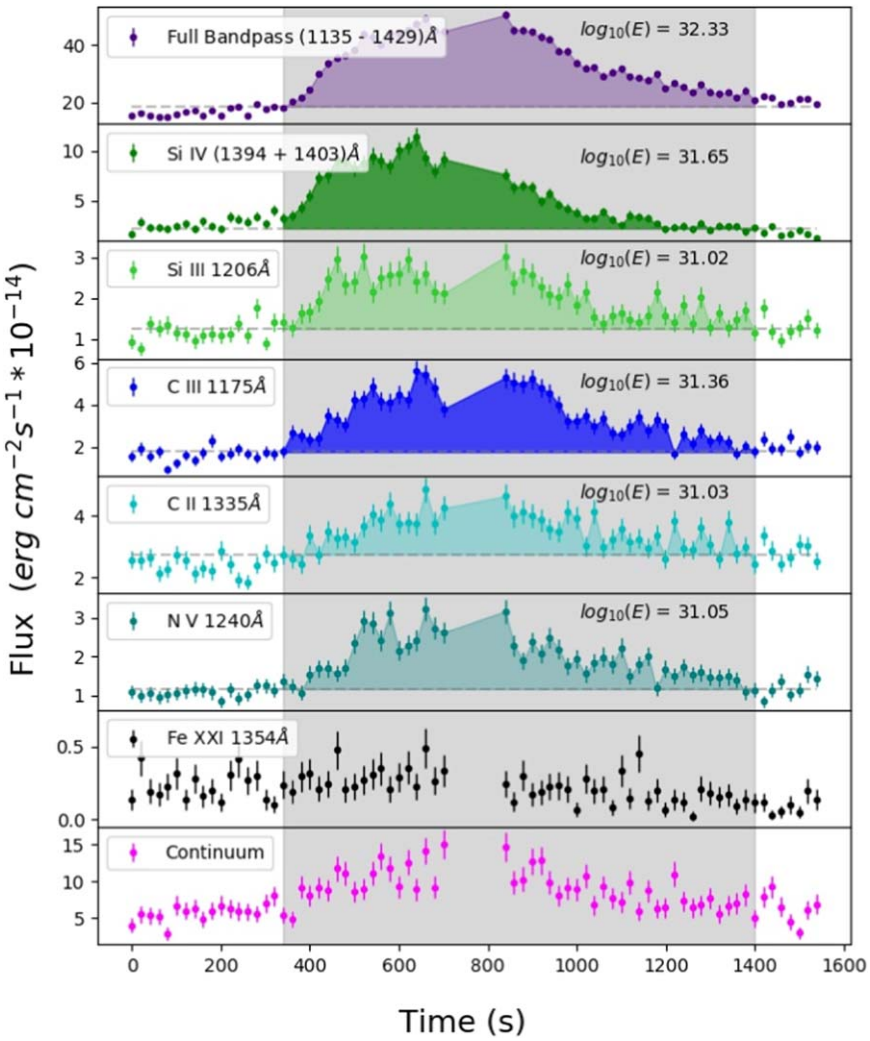

Figure 7. The first FUV flare observed on a WTTS (RECX-1). The gray shaded region is the manually identified flare ($\Delta t = 20$ s). There is a temporal gap between observations from 700 to 840 s. There is a weak response in the continuum and no detectable response in Fe XXI, which suggests that there is not an associated strong X-ray flare. Five bandpasses are used to compute the continuum light curve. They are 1146.8–1149.8 Å, 1156.2–1171.4 Å, 1181–1188.4 Å, 1248.3–1258.5 Å, and 1339–1351 Å.

Appendix D
Common Bandpass: TW Hya

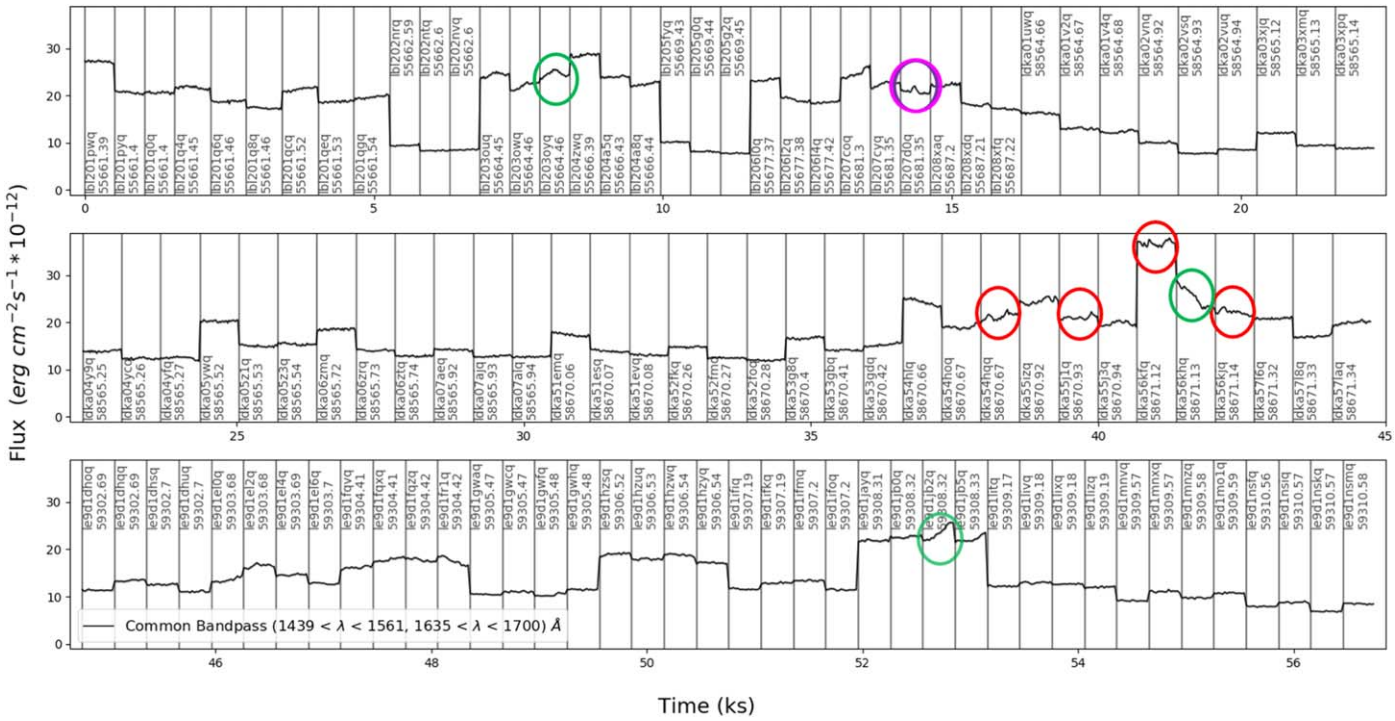

Figure 8. The full TW Hya light curve shown for the common STIS E140M and COS G160M bandpass ($\Delta t = 20$ s, 15.75 hr total). The error bars are plotted, but they are smaller than the width of the line. The flare shown in Figure 5 is encircled here in magenta. Note the fairly well behaved quiescence in this observation window, with the flare occurring in the middle of the observation. Four other possible flares are shown encircled in red, and rapid rise and decay activity is encircled in green. These red and green circled observations are too noisy to establish a quiescent level with confidence, but they contain noteworthy activity.

Appendix E
LCA Combing for Flares

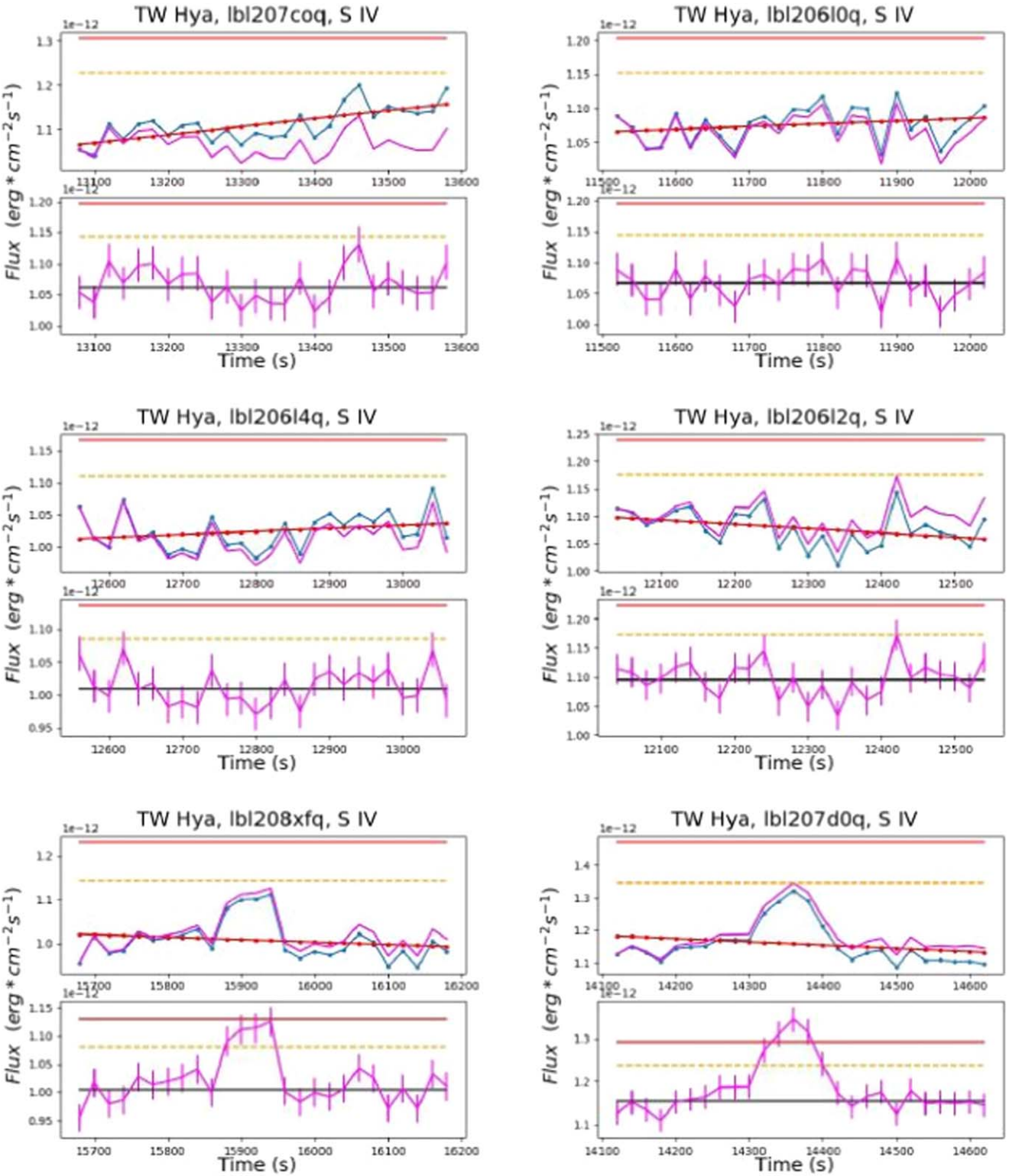

Figure 9. Each top panel shows the unadjusted data in blue, the slope-adjusted data in magenta, and the fit line in red. The slope-adjusted data are the unadjusted data corrected for the slope in the red line. Each bottom panel shows only the slope-adjusted data, with statistical levels (3σ: dashed orange; 5σ: solid red) computed ignoring potential flares. The plot title shows the target star, the HST ID, and the hot accretion line being analyzed.

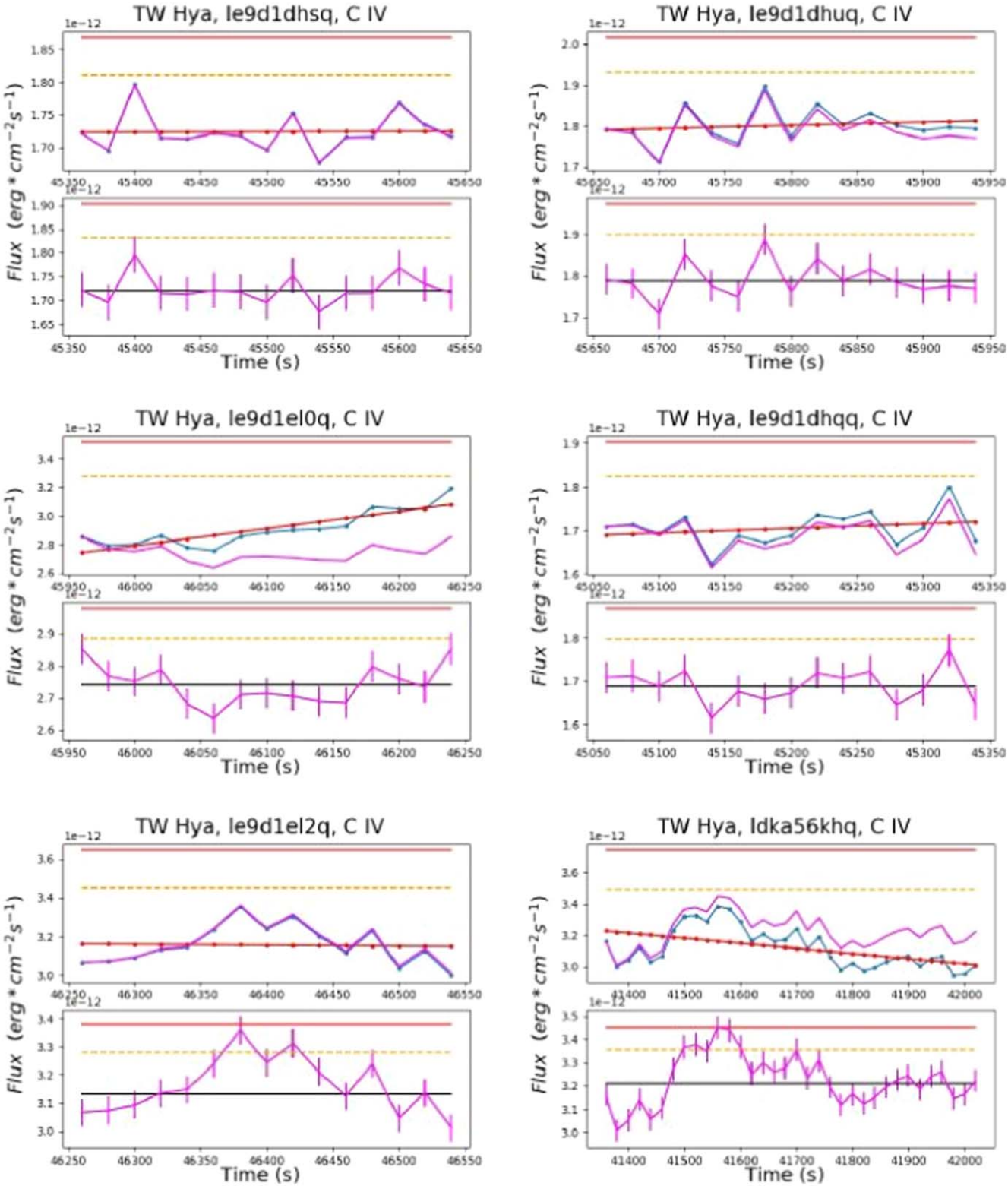

Figure 10. Each top panel shows the unadjusted data in blue, the slope-adjusted data in magenta, and the fit line in red. The slope-adjusted data are the unadjusted data corrected for the slope in the red line. Each bottom panel shows only the slope-adjusted data, with statistical levels (3σ: dashed orange; 5σ: solid red) computed ignoring potential flares. The plot title shows the target star, the HST ID, and the hot accretion line being analyzed.

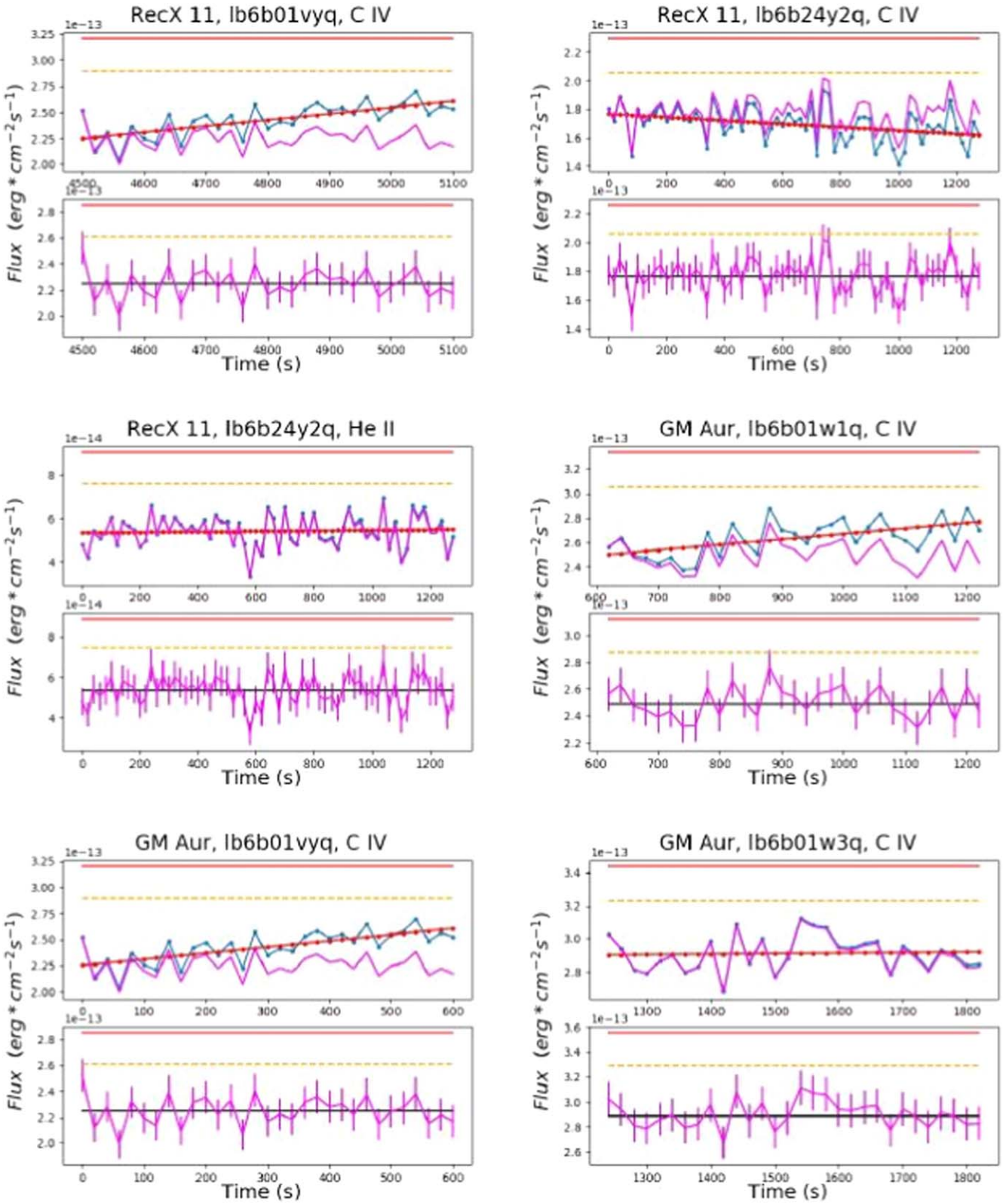

Figure 11. Each top panel shows the unadjusted data in blue, the slope-adjusted data in magenta, and the fit line in red. The slope-adjusted data are the unadjusted data corrected for the slope in the red line. Each bottom panel shows only the slope-adjusted data, with statistical levels (3σ: dashed orange; 5σ: solid red) computed ignoring potential flares. The plot title shows the target star, the HST ID, and the hot accretion line being analyzed.

Appendix F
TESS Example Flares

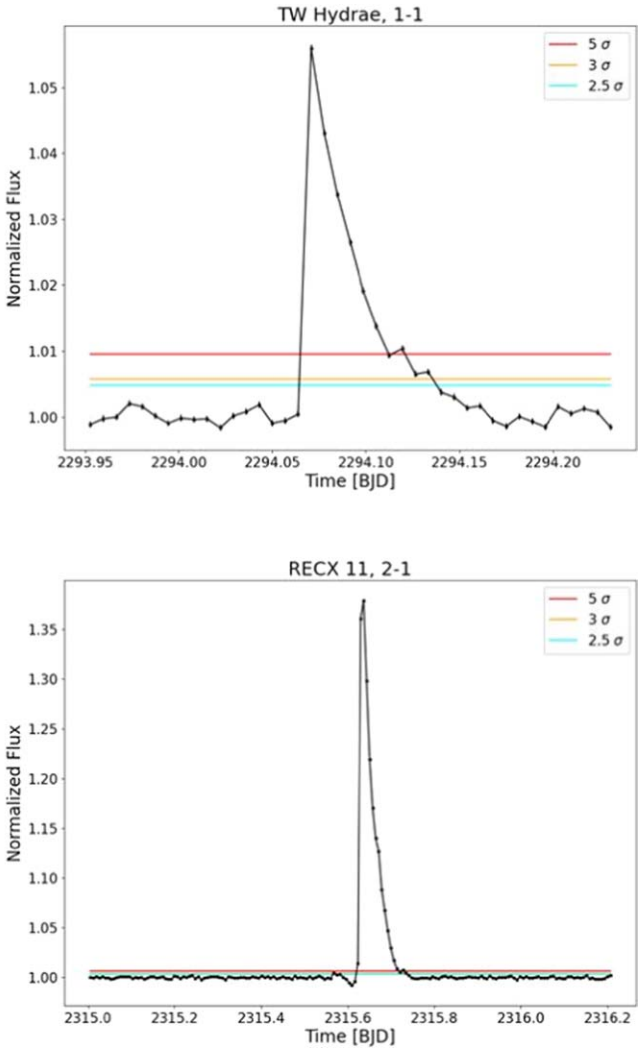

Figure 12. Two example TESS flares are shown: one from TW Hya (top) and one from RECX-11 (bottom). The flare IDs (1-1 and 2-1, respectively) can be compared with the corresponding rows in Appendix B for quantified flare parameters. For both energetic flares, the σ marker lines and the error bars are small compared with the flare's profile. This is especially the case for the REX-11 flare. Both flares follow the standard profile of fast rise and exponential decay.

ORCID iDs

P. C. Hinton https://orcid.org/0000-0001-9504-0520
Kevin France https://orcid.org/0000-0002-1002-3674
Javier Serna https://orcid.org/0000-0001-7351-6540
Jesús Hernández https://orcid.org/0000-0001-9797-5661
Hans Moritz Günther https://orcid.org/0000-0003-4243-2840
Adam F. Kowalski https://orcid.org/0000-0001-7458-1176
P. Christian Schneider https://orcid.org/0000-0001-7458-1176

References

Alexander, R., Pascucci, I., Andrews, S., Armitage, P., & Cieza, L. 2014, in Protostars and Planets VI, ed. H. Beuther et al. (Tucson, AZ: Univ. Arizona Press), 475
Ali-Dib, M. 2017, MNRAS, 464, 4282
Ansdell, M., Gaidos, E., Rappaport, S. A., et al. 2016, ApJ, 816, 69
Antonucci, E., Gabriel, A. H., & Dennis, B. R. 1984, ApJ, 287, 917
Ardila, D. R., Herczeg, G. J., Gregory, S. G., et al. 2013, ApJS, 207, 1
Binks, A. S., Jeffries, R. D., & Wright, N. J. 2020, MNRAS, 494, 2429
Brasseur, C. E., Phillip, C., Fleming, S. W., Mullally, S. E., & White, R. L. 2019, Astrocut: Tools for creating cutouts of TESS images, Astrophysics Source Code Library, ascl:1905.007
Bressert, E., Bastian, N., Gutermuth, R., et al. 2010, MNRAS, 409, L54
Clarke, C. 2011, The Dispersal of Disks around Young Stars (Chicago, IL: Univ. Chicago Press), 355
de la Reza, R., Jilinski, E., & Ortega, V. G. 2006, AJ, 131, 2609
Ercolano, B., & Pascucci, I. 2017, RSOS, 4, 170114
Espaillat, C. C., Herczeg, G. J., Thanathibodee, T., et al. 2022, AJ, 163, 114
Espaillat, C. C., Macías, E., Hernández, J., & Robinson, C. 2019, ApJL, 877, L34
Fox, A., James, B. L., Frazer, E. M., & Fischer, W. J. 2019, The Flux Calibration of the New COS/FUV Cenwave G160M/1533, Instrument Science Report COS 2019-9
France, K., Duvvuri, G., Egan, H., et al. 2020, AJ, 160, 237
France, K., Loyd, R. O. P., Youngblood, A., et al. 2016, ApJ, 820, 89
France, K., Schindhelm, E., Bergin, E. A., Roueff, E., & Abgrall, H. 2014, ApJ, 784, 127
Gaia Collaboration, Brown, A. G. A., & Vallenari, A. 2018, A&A, 616, 22
Gershberg, R. E. 1972, Ap&SS, 19, 75
Getman, K. V., & Feigelson, E. D. 2021, ApJ, 916, 32
Getman, K. V., Feigelson, E. D., & Garmire, G. P. 2021, ApJ, 920, 154
Getman, K. V., Feigelson, E. D., Micela, G., et al. 2008, ApJ, 688, 437
Gold, T., & Hoyle, F. 1960, MNRAS, 120, 89
Gorti, U., & Hollenbach, D. 2009, ApJ, 690, 1539
Gorti, U., Liseau, R., Sándor, Z., & Clarke, C. 2016, SSRv, 205, 125
Guillot, T., & Hueso, R. 2006, MNRAS, 367, L47
Gullbring, E., Gahm, G. F., Barwig, H., & Chen, P. 1995, in Proc.s of the IAU Coll. 151, Flares and Flashes, ed. J. Greiner, H. W. Duerbeck, & R. E. Gershberg (New York: Springer International), 221
Gullbring, E., Hartmann, L., Briceño, C., & Calvet, N. 1998, ApJ, 492, 323
Günther, M. N., Zhan, Z., Seager, S., et al. 2020, AJ, 159, 60
Hartmann, L., Calvet, N., Gullbring, E., & D'Alessio, P. 1998, ApJ, 495, 385
Hartmann, L., Herczeg, G., & Calvet, N. 2016, ARA&A, 54, 135
Hawley, S. L., Allred, J. C., Johns-Krull, C. M., et al. 2003, ApJ, 597, 535
Herczeg, G. J., & Hillenbrand, L. A. 2014, ApJ, 786, 97
Herczeg, G. J., Linsky, J. L., Valenti, J. A., Johns-Krull, C. M., & Wood, B. E. 2002, ApJ, 572, 310
Hilton, E. J., Hawley, S. L., Kowalski, A. F., & Holtzman, J. 2011, in ASP Conf. Ser. 448, 16th Cambridge Workshop on Cool Stars, Stellar Systems, and the Sun, ed. C. Johns-Krull, M. K. Browning, & A. A. West (San Francisco, CA: ASP), 197
Hueso, R., & Guillot, T. 2005, A&A, 442, 703
Ilin, E., Schmidt, S. J., Poppenhäger, K., et al. 2021, A&A, 645, A42
Ingleby, L., Calvet, N., Bergin, E., et al. 2011, ApJ, 743, 105
Ingleby, L., Calvet, N., Herczeg, G., et al. 2013, ApJ, 767, 112
Jackman, J. A. G., Wheatley, P. J., Pugh, C. E., et al. 2019, MNRAS, 482, 5553
Johns-Krull, C. M., Valenti, J. A., & Linsky, J. L. 2000, ApJ, 539, 815
Johnstone, C. P., Bartel, M., & Güdel, M. 2021, A&A, 649, A96
Johnstone, D., Hollenbach, D., & Bally, J. 1998, ApJ, 499, 758
Kiefer, F., Lecavelier des Etangs, A., Boissier, J., et al. 2014, Natur, 514, 462
Königl, A., & Salmeron, R. 2011, The Effects of Large-Scale Magnetic Fields on Disk Formation and Evolution (Chicago, IL: Univ. Chicago Press), 283
Kóspál, Á., Ábrahám, P., Zsidi, G., et al. 2018, ApJ, 862, 44
Kraus, A. L., & Hillenbrand, L. A. 2009, ApJ, 704, 531
Loyd, R. O. P., & France, K. 2014, ApJS, 211, 9
Loyd, R. O. P., France, K., Youngblood, A., et al. 2018a, ApJ, 867, 71
Loyd, R. O. P., Shkolnik, E. L., Schneider, A. C., et al. 2018b, ApJ, 867, 70
Luhman, K. L., & Steeghs, D. 2004, ApJ, 609, 917
McJunkin, M., France, K., Schneider, P. C., et al. 2014, ApJ, 780, 150
Medina, A. A., Winters, J. G., Irwin, J. M., & Charbonneau, D. 2020, ApJ, 905, 107
Mitra-Kraev, U., Harra, L. K., Güdel, M., et al. 2005, A&A, 431, 679
Neupert, W. M. 1968, ApJL, 153, L59
Parker, E. N. 1963, ApJS, 8, 177
Ricker, G. R., Winn, J. N., Vanderspek, R., et al. 2014, Proc. SPIE, 9143, 914320
Robrade, J., & Schmitt, J. H. M. M. 2006, A&A, 449, 737
Rodrigo, C., & Solano, E. 2020, The SVO Filter Profile Service (Spain: Spanish Astronomical Society)

Rodrigo, C., Solano, E., & Bayo, A. 2012, SVO Filter Profile Service Version 1.0, IVOA Working Draft 15, Spanish Astronomical Society, doi:10.5479/ADS/bib/2012ivoa.rept.1015R
Roman-Duval, J., Proffitt, C. R., Taylor, J. M., et al. 2020, RNAAS, 4, 205
Rosotti, G. P., Ercolano, B., Owen, J. E., & Armitage, P. J. 2013, MNRAS, 430, 1392
Schmitt, J. H. M. M., Ioannidis, P., Robrade, J., Czesla, S., & Schneider, P. C. 2019, A&A, 628, A79
Schneider, P. C., Eislöffel, J., Güdel, M., et al. 2013, A&A, 557, A110
Schneider, P. C., Günther, H. M., & France, K. 2020, Galax, 8, 27
Serna, J., Hernandez, J., Kounkel, M., et al. 2021, ApJ, 923, 177
Shibayama, T., Maehara, H., Notsu, S., et al. 2013, ApJ, 209, 5
Shkolnik, E., Liu, M. C., & Reid, I. N. 2009, ApJ, 699, 649
Shu, F. H., Johnstone, D., & Hollenbach, D. 1993, Icar, 106, 92
Stassun, K. G., Oelkers, R. J., & Paegert, M. 2019, AJ, 158, 21
Stelzer, B., Flaccomio, E., Briggs, K., et al. 2007, A&A, 468, 463
Teague, R., Bae, J., Huang, J., & Bergin, E. A. 2019, ApJL, 884, L56
Veronig, A. M., Brown, J. C., Dennis, B. R., et al. 2005, ApJ, 621, 482
Welsh, B. Y., Wheatley, J., Browne, S. E., et al. 2006, A&A, 458, 921
Wolk, S. J., Harnden, F. R. J., Flaccomio, E., et al. 2005, ApJS, 160, 423
Woodgate, B. E., Kimble, R. A., Bowers, C. W., et al. 1998, PASP, 110, 1183
Wright, J. T., Fakhouri, O., Marcy, G. W., et al. 2011, PASP, 123, 412
Zhu, C., Liu, R., Alexander, D., & McAteer, R. T. J. 2016, ApJL, 821, L29